seit 1558

Friedrich-Schiller-Universität Jena

Abbe School of Photonics

M.Sc. Photonics

Master's Thesis

Investigation of Pump-Induced Phase Aberrations for Solid-State Laser Amplifiers

Author:
Issa Tamer

Supervisor:
Prof. Dr. Malte C. Kaluza
Dr. Marco Hornung

November 11, 2016

Table of Contents

1   Introduction

Recent scientific endeavors in the realm of relativistic laser plasma physics benefit from the increase of the on-target intensity ($\gtrsim 10^{21} \frac{W}{cm^2}$) generated by a sufficiently powerful laser.[1] With such a laser system, the processes of ion[2] or electron[3] acceleration, laser-based x-ray generation,[4] high intensity laser physics,[5] and laser-based proton radiography[6] can be more adequately understood and improved towards higher particle energies. In order to further fuel the investigation of these interactions, the question remains as to how a state-of-the-art petawatt class laser system can be upgraded. Several paths can be taken to increase the intensity: through improved beam profiles via wavefront aberration corrections, higher energies, and shorter pulse durations. Although diode-pumped solid-state laser systems employing Yb^{3+}-doped active materials can achieve femtosecond pulses with energies in the Joule regime,[7] the focal spot intensity is nevertheless limited by the quality of the laser beam, resulting from strong phase distortions within the beam profile.

These phase aberrations are mainly a product of the optical pumping process of the active material, necessary in order to generate population inversion and optical gain. A percentage of the energy from the pump laser is translated into heat through non-radiative transitions, which results in a temperature increase and subsequent refractive index change, based on the dn/dT, photoelastic effect, and expansion of the material. A non-uniform change in the refractive index due to the intensity profile of the pump laser causes the incident wavefront of the seed laser to experience an additional, spatially and temporally varying, phase-shift. This effect, due to the temperature rise in the active material, is referred to as a "thermal lens". An additional type of aberration is also formed when a difference exists in the charge distribution of the dopant ion at different energy levels. Since this is based on the amount of population inversion encouraged by the pump, this spatiotemporal phase-shift effect is called a "population lens". Both of these aberrations affect the phase profile of the incident seed laser with comparable amplitudes, yet occur on difference time scales. Therefore, revealing the full behavior of the pump-induced phase aberrations in diode-pumped active materials requires a spatially and temporally resolved study. The investigation presented in this thesis accomplishes this through high-resolution interference measurements, gain measurements, and a thermal simulation with COMSOL, verified with a thermal imaging camera. The results of this characterization are intended to be applicable to a multitude of solid-state laser systems.

Investigations tailored towards improving the high peak power ultrashort laser

system POLARIS, located in Jena, Germany, are not only limited to the quality of the beam profile. An optical system can be built which is capable of testing multiple aspects of the laser amplification process. However, since the POLARIS[7] laser system is operational and continuously in use, testing out various changes delays research projects which depend on the stability of the system. In this sense, a standalone system, which can still be seeded with the POLARIS laser, is a clever way to test possible upgrades while keeping the original laser system active for research. A testbed amplifier can combine and test different amplification schemes and laser-active materials to determine which produces the best combination of gain, efficient energy extraction, spectral bandwidth, and resulting beam quality. A brief look at the POLARIS layout and specifications, described in the following section, is useful in determining which types of amplification schemes (regenerative, multi-pass, or relay-imaging) and active materials (Yb^{3+}-doped crystals or glass) could be used as a starting point for the testbed amplifier. Before placing the active materials in the testbed setup, a separate investigation should be held, since an in-depth (spatiotemporal) knowledge of the behavior of the employed active materials is an important step in generating high quality and high energy beams, and requires a large setup which cannot fit on one optical table in conjunction with the testbed amplifier. Once a satisfactory result is obtained with the standalone system, the changes can be applied to either an existing or an additional amplifier.

The topics that follow begin with a brief introduction on relevant key concepts. The subsequent section explains the design of the pump source utilized during this investigation and compares the measured and predicted thermal and population lenses found within three Yb^{3+}-doped active materials. The final topic of this thesis outlines the completion of an optical system which can be used to further observe these aberrations within normal amplifier operation and test relay-imaging vs multi-pass amplification, multiple active materials, and additional accessories utilized within amplifier stages, through multiple diagnostics. The combination of the pump source, active material, and amplifier design topics in this thesis grants a well-rounded insight into the field of diode-pumped solid-state laser systems.

2   Theoretical Concepts and Methods

2.1   Creating and Amplifying a Laser Pulse

The design, construction, and improvement of a high peak power ultrashort laser system requires the knowledge of a plethora of important concepts, several of which will be introduced through a brief explanation of the layout[8] of the POLARIS laser system, shown in figure 1 below.
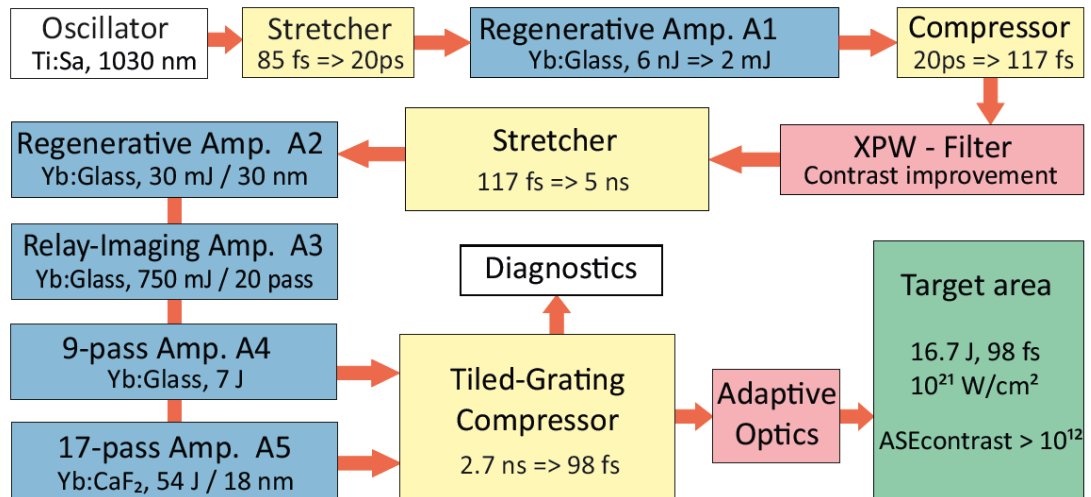

Figure 1: POLARIS schematic overview

POLARIS begins with an oscillator that forms a femtosecond laser pulse through a nonlinear self-focusing mechanism called the optical Kerr effect. An oscillator typically consists of a pump source, several mirrors to form an optical cavity structure, and an active material, which grants optical gain for a laser through stimulated emission. A vibrating glass plate is used to generate random phase-shifts within the longitudinal modes present in the laser cavity, until they align in phase and combine constructively, forming a short pulse. This pulse is focused by a curved mirror into an active material, generating intensities high enough to trigger self-focusing, since the refractive index of the chosen active material (Titanium-doped sapphire) exhibits an intensity-dependent refractive index. As the pulse gathers gain and undergoes further self-focusing, it passes through a hard aperture which blocks the larger diameter (non-self-focused, low-intensity) continuous wave operation. By introducing this intensity-dependent loss mechanism, the multiple longitudinal modes within the short pulse are locked together with a fixed phase relationship, allowing for femtosecond laser operation. This method of ultrashort pulse generation is referred to as "hard-aperture Kerr-lens modelocking", and is only one of several procedures utilized for the development of

laser pulses.[9] As the laser pulse exits the oscillator at high intensities, the strong probability exists of damaging subsequent amplifiers or optical components. For this reason, in a process referred to as Chirped Pulse Amplification (CPA),[10] the pulse is sent through a "stretcher", which temporally separates the longitudinal modes and decreases the pulse peak power (and therefore intensity). This allows for a safer amplification process, after which the pulse can be temporally compressed through a reversal of the previously-induced dispersion with the use of a grating or prism pair. The implementation of a cross-polarized wave generation (XPW) filter is important for applications where a high temporal intensity contrast is required, as only the high-intensity pulse (and not the lower-intensity pedestal) survives the nonlinear XPW process. After these steps, the laser pulse is ready for high energy amplification. It is important to note the damage thresholds of the materials used in the amplifiers, as this defines the fluence limit of the entire laser system ($\sim 3\,\mathrm{J/cm^2}$ for Yb:Glass and $\sim 7\,\mathrm{J/cm^2}$ for Yb:CaF$_2$ in POLARIS).

The quality of a laser amplifier is governed by the interplay between pump fluence and saturation fluence, which eventually translates into a contest between gain and energy extraction. Key quantities for consideration when modeling the amplification process are the pulse energy E, fluence (Energy/Area) J, and small signal gain g_0. The small signal gain is dependent on the level of population inversion within the active material and represents the available optical gain when little or no signal is present. Through the use of a strong pump with a fluence $J_p = \frac{E_p}{A_p}$, where E_p and A_p are the pump energy and area respectively, the small signal gain can be increased, as more ions in the material are excited to the desired higher energy state. The pump fluence stored[11] in the active material $J_{sto} = \eta_\alpha \cdot \frac{\lambda_p}{\lambda} \cdot J_p$, which is released through either stimulated or spontaneous emission, is dependent on the percentage of absorbed pump photons η_α and the quantum defect $\frac{\lambda_p}{\lambda}$. The quantum defect is a non-negligible effect attributed to energy loss through non-radiative transitions, due to the difference in wavelength of the pump (λ_p) and seed (λ) lasers.

An incident laser, when sent through the material, acquires more photons through the wavelength-dependent stimulated emission process. As the number of photons which induce the stimulated emission process in the material increase, the available gain decreases. The laser fluence at which the available gain ($g = \frac{g_0}{1+\frac{J}{J_{sat}}}$) is reduced to half of the small signal gain is defined as the saturation fluence, which is material-dependent and a characteristic parameter of every amplifier: $J_{sat} = \frac{\hbar\omega}{\sigma}$, where $\hbar\omega$ is the photon energy and σ is the effective emission cross-section of the material. When a laser with a very low pulse energy is sent through an active material with length L, it can be assumed that the number of photons is not

high enough to perturb the value of the gain with respect to the small signal gain $(g_0 L = \frac{J_{sto}}{J_{sat}})$. Therefore, it is natural to define the change in fluence of the laser in the active material, within this limit,[11] as increasing linearly with z (axis of propagation through the material): $\frac{dJ}{dz} = g_0 J$. By solving for the output fluence, a formula for the initial gain factor G_0 of the active material is derived:

$$J_{out} = J_{in}e^{[g_0 L]} = J_{in}e^{\left[\frac{J_{sto}}{J_{sat}}\right]} = J_{in}G_0. \tag{1}$$

For higher pulse energies, the effect of saturated gain is taken into account through

$$\frac{dJ}{dz} = g_0 J_{sat}\left(e^{\left[\frac{J_{in}}{J_{sat}}\right]} - 1\right), \tag{2}$$

with the solution for the output fluence given by the Frantz-Nodvick equation:[11]

$$J_{out} = J_{sat}\ln\left[G_0\left(e^{\left[\frac{J_{in}}{J_{sat}}\right]} - 1\right) + 1\right]. \tag{3}$$

The ratio of $\frac{J_{in}}{J_{sat}}$ is plotted in figure 2 against J_{out}, revealing the interplay between gain $(\frac{J_{out}}{J_{in}})$ and extraction efficiency $(\frac{J_{out}-J_{in}}{J_{sto}})$.
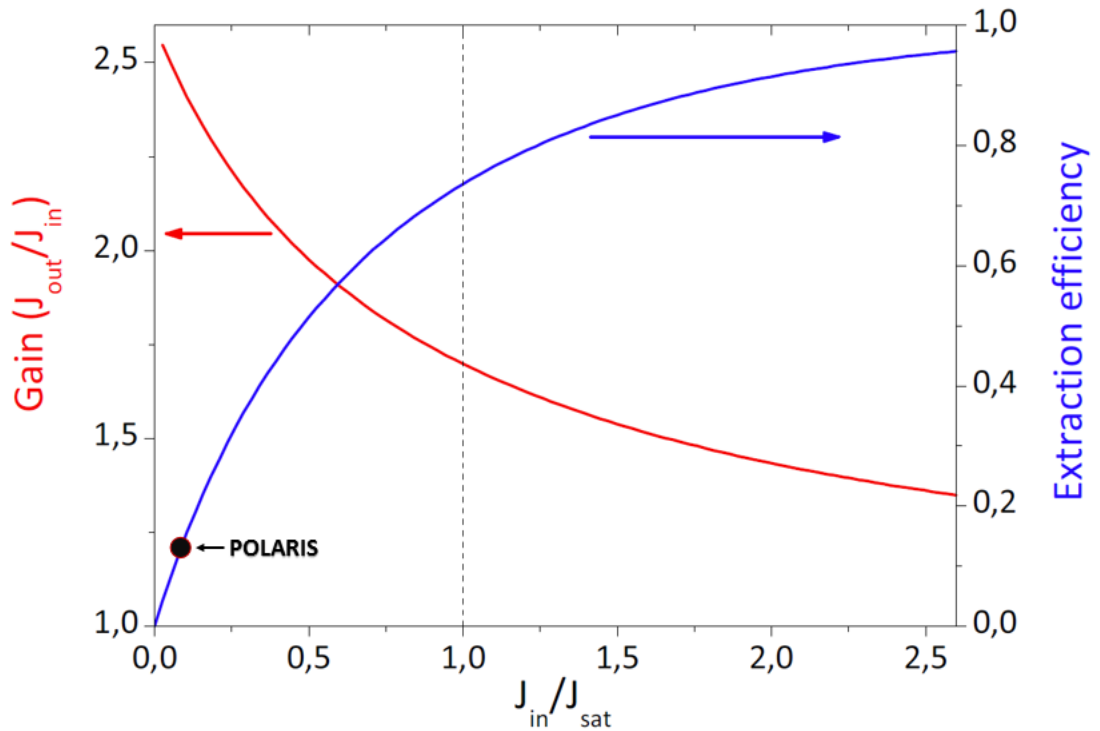

Figure 2: Interplay between gain and extraction efficiency,[13] along with the relevance of this relationship with respect to the Joule-class amplifiers in the POLARIS laser system $(\frac{J_{in}}{J_{sat}} \sim 0.1)$.

The Frantz-Nodvick equation therefore dictates that the non-saturated regime $J \ll J_{sat}$ results in a high gain (the ratio of output over input fluence), while

operating the laser in saturation $J \approx J_{sat}$ provides a high extraction efficiency (the amount of pump fluence that is translated into output fluence). For laser amplifiers operating at a high input fluence, it is desirable to find a material with a large saturation fluence to obtain a sufficient gain. For this reason, solid-state media (Yb:Glass with $J_{sat} \sim 50\,J/cm^2$ vs. dyes with $J_{sat} \sim 1\,mJ/cm^2$)[11] are widely used in present-day laser amplifiers. As the POLARIS system is limited by the low damage threshold of the active materials, the entire laser chain is in the non-saturated regime, since Yb^{3+}-doped materials with high saturation fluences are used. Amplifier designs with many passes are therefore needed through the active material to extract a sufficient amount of the pump energy.

2.1.1   Amplifier Designs for High Peak Power Laser Systems

When designing an amplifier for a high power laser system, choosing the best combination of pump, active material, and amplifier design is critical for maximizing the output energy. Designs that have been successful in exhibiting sufficient amplification of high energy pulses are the regenerative, multi-pass, and relay-imaging amplifiers. Basic illustrations can be seen in figure 3, immediately followed by a brief comparison of these laser systems.
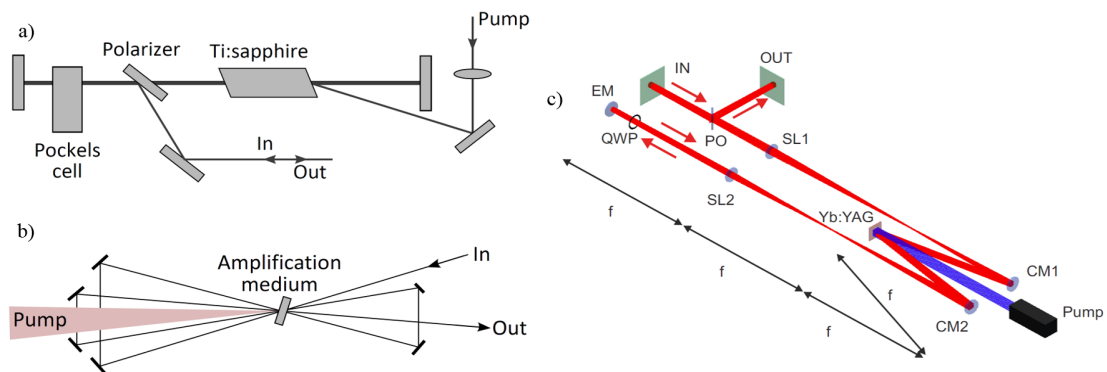
Figure 3: Schematic illustrations of a) regenerative[11] b) multi-pass[11] and c) relay-imaging[12] amplifier designs.

The regenerative amplifier consists of an optical resonator which allows for many round trips, leading to a high total gain. When sufficient energy has been extracted, the pulse is coupled out via a Pockels cell + polarizer setup. An optical isolator is used to separate the incoming and outgoing beams. This design suffers from dispersion due to many passes through the gain medium (which results in temporal broadening), and the generation of satellite pulses due to surface reflections and a limited Pockels cell extinction ratio, which are also amplified after the multiple round trips. At high energies the beam size must be increased to ensure that the input fluence is below the damage threshold. When certain properties

of the transverse mode (beam waist, Rayleigh range, and radius of curvature of the wavefront) cannot be supported by the laser cavity (with a defined length and radius of curvature of the mirrors), the resonator becomes unstable. Amplifier types which do not rely on a resonator structure can be added to the laser system chain to further amplify the large aperture beam before it is recompressed into a femtosecond pulse.

The multi-pass amplifier consists of a series of mirrors oriented around the active material in a carefully aligned bowtie-like structure, which provides the geometry needed for the series of passes. It is operated at a very high input energy and large diameter (the amplified output fluence is near the damage threshold), resulting in a lower gain but higher extraction efficiency. For this reason, the multi-pass amplifier is typically placed at the end of the set of amplifier stages for a high power laser system.

The relay-imaging amplifier is a variation of the multi-pass amplifier which mitigates typical issues that occur when amplifying high fluence pulses. The laser pulse in a multi-pass amplifier propagates through 10s of meters during the amplification process and may pass through multiple optics, leading to a deformation or aberration of the initially sharp beam profile. This negative effect can be corrected by imaging the beam at regular intervals (through the use of a telescope), in an effort to preserve a high beam quality throughout multiple passes. When a relay-imaging amplifier is designed for operation at intensities larger than $\sim 10^{13}\,\mathrm{W/cm^2}$, the entire amplifier must be placed in vacuum to avoid ionizing the surrounding air due to an intermediate image plane within the telescope layout.

2.1.1.1   The Relay-Imaging Amplifier

The use of curved mirrors within the relay-imaging amplifier design offers a variable number of passes through the active material via angle-tuning. For this reason, the testbed amplifier (revealed in chapter 4) begins with a relay-imaging setup. An analytical model can be developed for this optical system which utilizes a matrix formalism of geometrical optics in the paraxial approximation, with results equivalent to that of the ray-tracing equations. With this approach,[16] simple matrices are constructed for the transfer of a given optical ray in free space ($\mathrm{T} = \left[\begin{smallmatrix} 1 & d \\ 0 & 1 \end{smallmatrix}\right]$) through a distance "d", and a refraction of the optical ray via a thin lens ($\mathrm{L} = \left[\begin{smallmatrix} 1 & 0 \\ -\frac{1}{f} & 1 \end{smallmatrix}\right]$) with a focal length "f".

Consecutive products of the transfer and refraction matrices can be described by one matrix "M" for the entire optical system with "n" imaging elements. For "1:1 relay-imaging" to be fulfilled, the ray height (r) and angle (θ) with respect to the optical axis must have the same magnitudes at the start and end of the optical

system, while the sign depends on the handedness of the system. This simplifies the analytical model

$$
\begin{bmatrix} r \\ \theta \end{bmatrix}_{end} = M \cdot \begin{bmatrix} r \\ \theta \end{bmatrix}_{start}, \tag{4}
$$

since the optical matrix M can be set equivalent to the identity matrix:[14]

$$
M = T_{n+1} \cdot L_n \cdot T_n \cdot L_{n-1} \cdot T_{n-1} \cdot ... L_1 \cdot T_1 = \pm \begin{bmatrix} 1 & 0 \\ 0 & 1 \end{bmatrix}. \tag{5}
$$

Within the application of the relay-imaging concept for laser amplifier stages, two unique cases follow: type I (even) and type II (odd), shown in figure 4. The former can be described as a 4f-telescope sandwiched by two mirrors, such that the incident laser passes through the telescope twice per round trip. The latter consists of 3 imaging elements, with spacings such that an image of the beam is formed on the second optic and on the desired image plane.
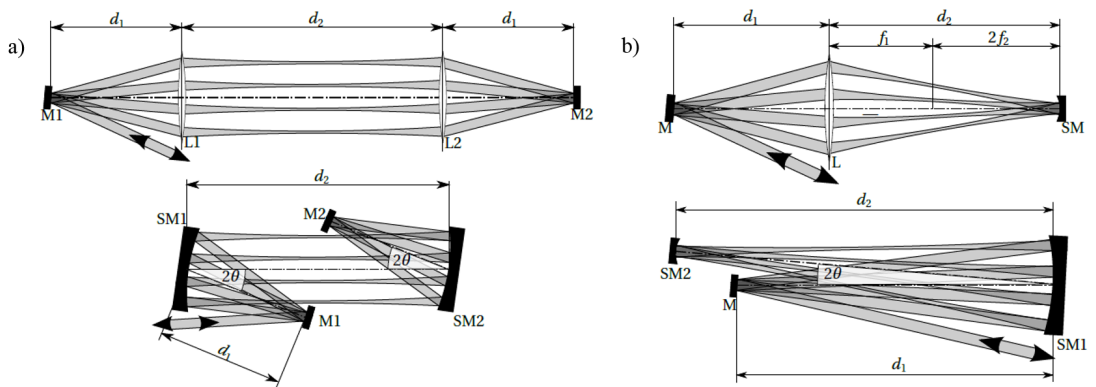

Figure 4: Unfolded (lenses) & folded (mirrors) for a) type I and b) type II relay-imaging amplifier designs.[14]

Both designs can be folded by replacing the lenses with curved mirrors, result-ing in a more compact setup and a removal of back-reflections (Fresnel reflections) or nonlinear effects (particularly wavefront and spectral phase distortions caused by a large B-integral value at high intensities) from the lenses. The disadvantage to folding the optical system is that a certain amount of astigmatism will be gener-ated, dependent on the folding angle and the number of round trips. Astigmatism due to the non-zero pitch angle to the optical axis, required for the angular sep-aration of each round trip, is additionally present in both unfolded and folded designs. A type II relay-imaging setup was chosen for the testbed amplifier due to its reduction in astigmatism by roughly a factor of two, when compared to the type I design.[14] This can be further mitigated by reducing the coupling angle into

the system and the folding angle of the relay-imaging design itself. By enforcing a folded, symmetric layout, the number of unknown variables in the aforementioned matrix model can be reduced considerably.

An unfolded type II system can be modeled with focal lengths $f_1 - f_3$ for each imaging element, along with corresponding distances $d_1 - d_4$. The folded version invokes the relationships $f_3 = f_1$, $d_3 = d_2$, and $d_4 = d_1$. This leads to the following construction of the optical system matrix

$$M = \frac{-1}{f_1^2 f_2} \cdot$$

$$
\begin{bmatrix}
\begin{array}{c} d_1 \cdot (d_2 - f_1) \cdot (d_2 - f_1 - 2f_2) \\ - f_1 \cdot (d_2^2 + f_1 f_2 - d_2 \cdot (f_1 + 2f_2)) \end{array} & \begin{array}{c} (d_1 \cdot (d_2 - f_1) - d_2 f_1) \cdot (-f_1 \cdot (d_2 - 2f_2) \\ + d_1 \cdot (d_2 - f_1 - 2f_2)) \end{array} \\[2em]
(d_2 - f_1) \cdot (d_2 - f_1 - 2f_2) & \begin{array}{c} d_1 \cdot (d_2 - f_1) \cdot (d_2 - f_1 - 2f_2) \\ - f_1 \cdot (d_2^2 + f_1 f_2 - d_2 \cdot (f_1 + 2f_2)) \end{array}
\end{bmatrix}
\tag{6}
$$

for the type II relay-imaging setup.[14] With an equal number of variables and equations, this system ($M = \begin{bmatrix} 1 & 0 \\ 0 & 1 \end{bmatrix}$) can be solved for the appropriate focal lengths

$$f_1 = d_2 - 2f_2 \tag{7}$$

$$f_2 = \frac{d_2^2}{2(d_1 + d_2)} \tag{8}$$

and distances

$$d_1 = \frac{f_1^2 + 2f_1 f_2}{2f_2} \tag{9}$$

$$\frac{1}{d_2} = \frac{1}{f_1} - \frac{1}{d_1}. \tag{10}$$

The values chosen for parameters f_1, f_2, d_1, and d_2 must follow the relationships detailed in equations 7 - 10 in order to maintain 1:1 imaging. It is noteworthy to mention that the imaging equation appears (equation 10) in the solution set, revealing that an image of the beam profile is also formed on the second folding mirror (SM2 in figure 4b), which is a distance d_2 away from the first folding mirror (SM1). The plane of SM2, where an image of the beam profile should form, can therefore be used to ensure that the optical system is aligned properly. The details regarding the realization of the testbed amplifier, which utilizes the model above, are continued in chapter 4.

2.2   Characteristic Properties of Yb^{3+}-doped Materials

Choosing the optimum active material(s) largely influences the ability of a laser system to be suitable for its designated application. A high peak power ultra-short laser system, such as POLARIS, can benefit greatly from materials exhibiting a broad emission spectrum (large enough to support the bandwidth of the seed pulse), a tight absorption spectrum (for efficient absorption from a narrow-bandwidth laser diode source), a longer radiative lifetime (such that the absorbed pump energy is stored for a longer period of time), and a reduced chance of parasitic effects. These advantages are obtainable when using the rare-earth ion dopant "ytterbium" (Yb^{3+}), making Yb^{3+}-doped materials especially attractive for diode-pumped solid-state laser (DPSSL) systems.

Figure 5: Yb^{3+} energy level diagram with typically employed manifolds.

The Yb^{3+} ion contains an electronic level structure with just two manifolds $^2F_{5/2}$ and $^2F_{7/2}$ (upper and lower lasing levels respectively), shown in figure 5, producing the typical center-wavelength emission of 1030 nm. The radiative lifetime of the upper (excited-state) lasing level of Yb^{3+}-doped materials (Yb:CaF$_2$ $\sim$ 2 ms) can allow for a significant buildup of population inversion (through the transfer of the energy state of the laser-active ion from the lower lasing level to the upper lasing level) with a lower pump power than typically required for other commonly employed laser-active materials (such as Ti:Sapphire, with a lifetime $\sim$ 3.7 μs). The necessary energy can be delivered over a longer pump pulse duration with laser diode pump sources instead of the more costly flash-lamps. Disadvantages of Yb^{3+} include the overlap of absorption and emission bands, leading to reabsorption, and the small energy separation between the multiple level splittings of the lower lasing level, which results in an increase in thermal population as the temperature of the material increases, reducing the available inversion. Cooling of the Yb^{3+}-doped active materials is therefore useful to maintain sufficient performance and avoid undesired effects.[19]

Doping a host material involves replacing a certain small percentage of atoms within the material with the dopant ion, in order to combine the lasing properties of the dopant with the ability of the host to manage the incident heat load. The dopant concentration is typically optimized in order to avoid detrimental effects such as quenching, due to additional energy transfer processes that may arise when laser-active ions cluster together or when impurities exist within the doped material. The side-effect is a decrease in the lifetime of the upper lasing level,[20] leading to a reduction of the time in which population inversion can be significantly built, and therefore a reduction of the gain in the active material.

The host material must also be wisely chosen, depending on the specific needs of the laser system, since the gain spectrum of the material is determined by the ion environment provided by the host. A structured arrangement of atoms within the host, characteristic of crystals, typically imbues materials with a high thermal conductivity and a narrower spectrum.[19] In this case, the laser-active ions within the lattice observe the same static fields, which homogeneously broaden the linewidth of the transition between the upper and lower lasing levels. This effect becomes larger with a mismatch in size between the dopant ion and the replaced ion, causing stronger static fields and a further broadening of the linewidth. An arrangement with a high disorder, such as glasses, exhibits lower thermal conductivity but a wider spectrum, due to inhomogeneous linewidth broadening occurring when the ions are subjected to different environments within the lattice.

Figure 6 displays the emission and absorption spectra of three prominent Yb^{3+}-doped active materials used in high power ultrashort laser systems: Yb:YAG (crystal), $Yb:CaF_2$ (mismatched crystal), and Yb:FP15 (fluorophosphate glass, also denoted simply as Yb:Glass). The emission and absorption cross-sections map the probability of photon emission or absorption onto a unit of area, and can be used to calculate the population inversion within a pumped active material:[14]

$$G = \exp\left[L{\cdot}N_{tot}{\cdot}\left(\frac{\Delta N}{N_{tot}}{\cdot}\sigma_e - \left[1 - \frac{\Delta N}{N_{tot}}\right]{\cdot}\sigma_a \right)\right]. \tag{11}$$

The gain factor (G) is denoted as the ratio of output over input energy of the laser passing through the active material. $N_{tot}\left[\frac{\text{ions}}{\text{cm}^3}\right]$ is the population of all of the relevant laser levels for the dopant ion (Yb^{3+}). The thickness (along the seed/pump propagation directions) of the active material is L [m], and $\Delta N \left[\frac{\text{ions}}{\text{cm}^3}\right]$ is the population inversion, which describes the density of ions in the upper lasing level of the Yb^{3+}-doped active material. Reabsorption of the emitted photons is included in the equation above, due to the overlap of emission and absorption spectra in Yb^{3+}-doped active materials.
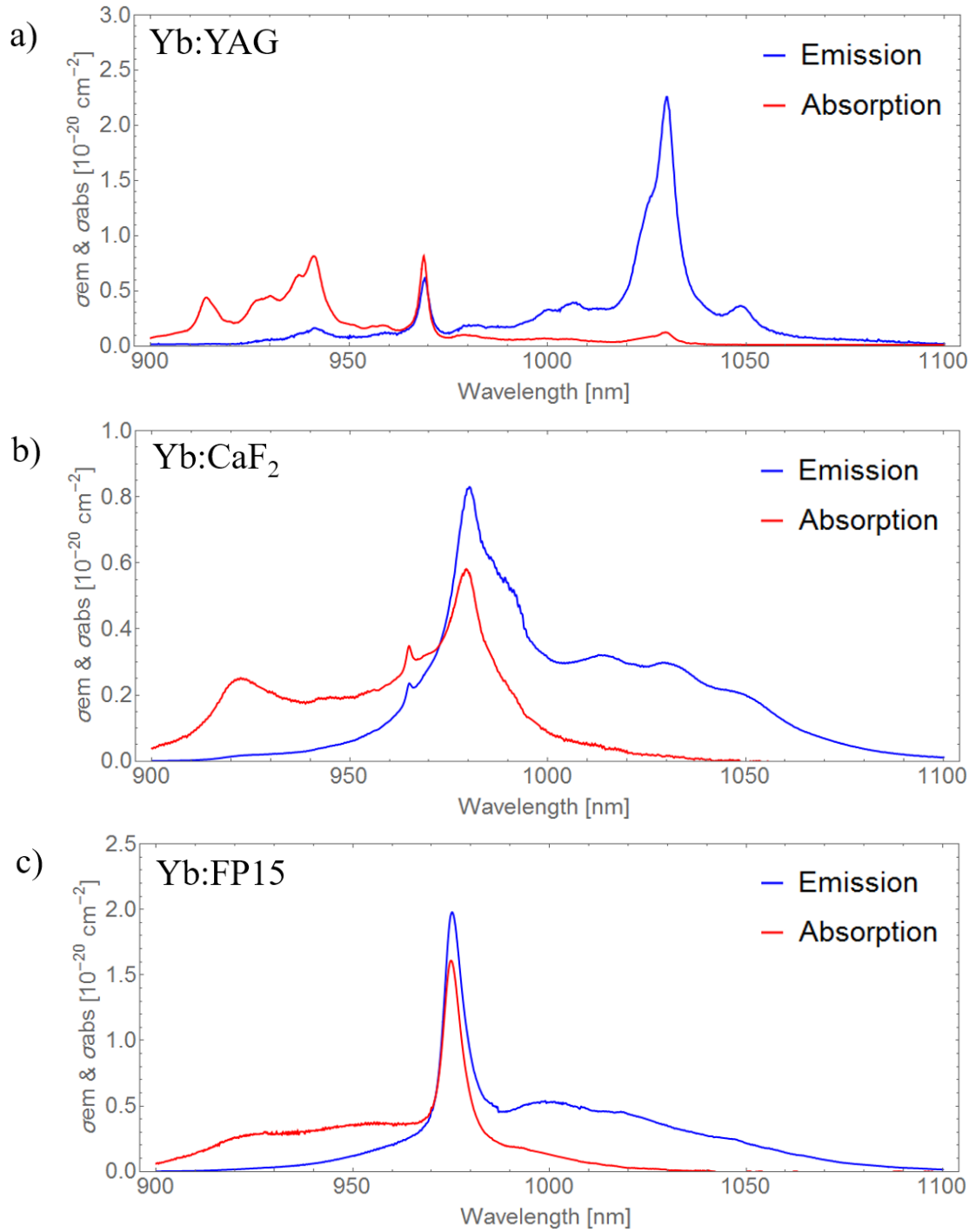
Figure 6: Comparison of the wavelength-dependent emission ($\sigma_e\,[cm^2]$) and absorption ($\sigma_a\,[cm^2]$) cross-sections for various Yb^{3+}-doped host materials.[17]

2.3   The Thermal Lens

Laser systems operating in the petawatt regime naturally require pump sources containing high pulse fluences to generate significant population inversion within the material and amplify an incoming high energy seed pulse. A side-effect of pumping an active material is an increase in temperature, mainly due to the quantum defect. Regardless of the complexity of the cooling system designed for the material, there will always be some thermal gradient formed between the pumped, unpumped, and directly cooled areas of the material. The combination of an inevitable inhomogeneous temperature rise (even with a homogeneous pump!) and mounting conditions will result in a change in the refractive index profile, depending on the absorbed heat load and the thermal and stress management properties of the host material. This pump-induced refractive index profile is referred to as a "thermal lens" and results in a phase imprint from the active material onto the seed laser. The thermal lens can be defined as a superposition of three material traits: a temperature-dependent refractive index, a stress-dependent refractive index (photoelastic effect), and the expansion of the material during the pumping process.[19] A positive thermal lens, which exhibits a higher refractive index in the center than on the outer edges of the material, retards wavefronts in the center of the seed beam more strongly than the outer edges, causing the beam to converge, much like it would when passing through a positive lens. If left uncompensated, this leads to focusing, significantly increasing the fluence and therefore the probability of laser-induced damage on optical components in the beam path. The opposite case, called a negative thermal lens, can also occur when the refractive index change is such that the refractive index in the center of the pumped area is less than that of the outer edges. The beam would then diverge, much like it would via a negative lens, resulting in a decrease in laser fluence and eventual clipping by the edges of optics in the beam path, in the case that the beam diverges too strongly.

Several assumptions were made to reduce the complexity of predicting the refractive index changes attributed to the thermal lens in the active material. The end-pumping configuration allows a plane stress approximation, useful for estimating the component of the induced phase-shift caused by the photoelastic effect.[21] Additional assumptions include the case of isotropic materials (fulfilled by the choice of YAG, CaF_2, and FP15 glass), a homogeneous and symmetric pump profile (fulfilled by the pump engine), and the neglecting of pump divergence (the pump size will not significantly change after passing through the material, which has a thickness on the order of some millimeters). The incident seed pulse would experience this inhomogeneous phase-shift (a phase-shift profile) as it propagates

through the material, and so the refractive index change must be integrated in the direction of propagation along the material length. With these approximations in play, the thermal lens profile can be estimated by the following phase-shift profile function $\phi(r)$, for a period in time in which the temperature profile is known:[19]

$$\phi(r) = \left[\frac{dn}{dT} + 2n_0^3\alpha_T C_r' + (n_0 - 1)(1 + \nu)\alpha_T \right] \int_0^L (T(0,z) - T(r,z))\,dz. \quad (12)$$

In equation 12, the first component within the squared brackets is the change in refractive index n with respect to the temperature T. The second component is attributed to the photoelastic effect, which describes the change in the shape of the dielectric impermeability tensor in the linear regime, and therefore the change in the refractive index due to stress. The stress in the material is compressive, since the cooler outer edges of the material act against the expansion from the center. The photoelastic constant C_r' along the radial direction can be calculated from a reduced form of the elasto-optic tensor, when Poisson's ratio and the elasto-optical coefficients of each material[19][27][30] p_{11} & p_{12} are known, via[21] $C_r' = \frac{-(1+\nu)(9p_{11}+15p_{12})}{48}$. The third component within the squared brackets deals solely with the expansion of the material, which is dependent on Poisson's ratio ν, the coefficient of thermal expansion α_T, and the value of the initial refractive index n_0 of the material at the input laser wavelength. The summation of the components within the brackets forms a value typically in the range of $\pm 10^{-6}\,K^{-1} \sim \pm 10^{-5}\,K^{-1}$. For the case of unextreme temperature increases ($\Delta T \sim 10\,K$) and an incident wavelength in the VIS-NIR, maximum phase-shifts can be expected to remain in the nanometer regime within the pump cycle. After the pump shot has passed, the phase-shift profile characteristic of the thermal lens will relax slowly as the material cools, according to the thermal conductivity and specific heat capacity values.

2.3.1   Thermal Profile Simulation

Predicting the magnitude and temporal behavior of the thermal lens requires a model of the temperature profile throughout the pumped material, which can be accomplished through the use of a finite element analysis software. COMSOL is an example of such a software, and grants the user the ability to build a 3D model of the pumped active material and solve the time-dependent heat transfer equation

$$\rho C_p \frac{\partial T(x,y,z,t)}{\partial t} - K_{th}\nabla^2 T(x,y,z,t) = Q_{th}(x,y,z,t) = \eta I(x,y,t)\alpha e^{-\alpha z}, \quad (13)$$

which predicts the flow of heat through a material via conduction,[19] based on the given pump conditions.

A closer look at the individual components of the equation grants an insight into how the material parameters contribute to the thermal profile $T(x, y, z, t)$ of the material. The coordinate system is set such that the xy-plane is parallel to the face of the material (where the pump meets the active material), while the z-plane runs along the material thickness. The first term on the left-hand-side of the equation shows that the temperature variation in the pulsed regime is affected by the density $\rho \left[\frac{kg}{m^3}\right]$ and specific heat capacity $C_p \left[\frac{J}{kg \cdot K}\right]$ parameters. The thermal conductivity $K_{th} \left[\frac{W}{m \cdot K}\right]$ affects the magnitude of the temperature gradient in the material, making this a value of particular importance when dealing with the thermal lens effect. The term on the right-hand-side is the thermal load $Q_{th} \left[\frac{W}{m^3}\right]$, which can be described as the "absorbed power density" of a heat source. The heat source in this investigation is that of the pump engine with intensity $I(x, y, t)$, and is modeled as a laser pulse train with a rectangular spatial and temporal profile. The absorption $\alpha \left[\frac{1}{m}\right]$ (dependent on the dopant concentration) of the material and the percentage of energy transferred to heat due to the quantum defect η (along with other non-radiative transitions due to material impurities) plays a key role in determining the strength of the thermal load. The energy contained within the pump laser while propagating through the material can be described by an exponential decay according to Beer-Lambert. An example of the 3-D pump profile can be observed by capturing an image of the fluorescence light, displayed in figure 7.
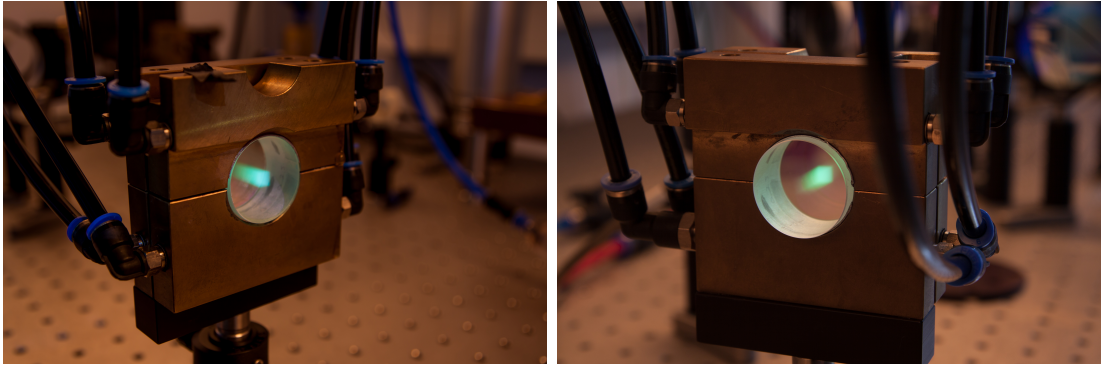

Figure 7: Images of the front (left) and back (right) sides of a weakly-pumped CaF_2 crystal. Although the pump laser is in the infrared, some of the fluorescence light is visible (green) due to laser transitions made available by dopant impurities within the active material.

Variations in the operating temperature, manufacture processes, and doping concentration (Yb:YAG: $4.2 \cdot 10^{20} \frac{\text{ions}}{\text{cm}^3}$, Yb:CaF$_2$: $3.8 \cdot 10^{20} \frac{\text{ions}}{\text{cm}^3}$, Yb:FP15: $6 \cdot 10^{20} \frac{\text{ions}}{\text{cm}^3}$) influence not only the optical properties (e.g., the spectrum, upper lasing level lifetime, and refractive index) properties of the active materials, but the thermal management capabilities (displayed in table 1 for the tested materials) as well.

Table 1: Relevant optical and thermal properties of the tested active materials.

Material	$K_{th}\left[\frac{W}{m\cdot K}\right]$	$\rho\left[\frac{kg}{m^3}\right]$	$\alpha_T\left[\frac{1}{K}\right]$	$C_p\left[\frac{J}{kg\cdot K}\right]$	$\frac{dn}{dT}\left[\frac{1}{K}\right]$	$\alpha\ \left[\frac{1}{m}\right]$
Yb:YAG[14][19]	9.2	4660	$6.1\cdot10^{-6}$	590	$10\cdot10^{-6}$	232.7
Yb:CaF$_2$[14][28][27]	9.71	3180	$18.4\cdot10^{-6}$	854	$-10.6\cdot10^{-6}$	67
Yb:FP15[14][31]	0.88	4560	$14\cdot10^{-6}$	720	$-8.6\cdot10^{-6}$	187

The thermal conductivity K_{th}, specific heat capacity C_p, density ρ, and pump beam radius w_p can be used to give an approximate value for the characteristic timescale of the relaxation of the temperature increase per pump pulse,[30] which will be referred to as the thermal diffusion time ("D" is the thermal diffusivity):

$$\tau_D = \frac{w_p^2}{4\cdot D} = \frac{w_p^2\cdot C_p\cdot\rho}{4\cdot K_{th}}. \tag{14}$$

A high spatiotemporal resolution can be accomplished, while reducing the risk of the thermal profile simulation crashing due to insufficient computer memory, through the use of meshing techniques and temporal event structures. A custom meshing gradient was defined for the modeled active material, such that the area within the pumped region was split into a high concentration of tessellations (the heat-transfer equation is solved for each of these components), and the area outside the pumped regions contained a lower concentration of tessellations. With temporal event structures, the simulation could choose the most appropriate time steps (within certain limits) for its subsequent calculations of the heat transfer equation, except for the explicit occurrence of a predefined event. The events for the case of this investigation are the periodic on/off times for the pump pulse.
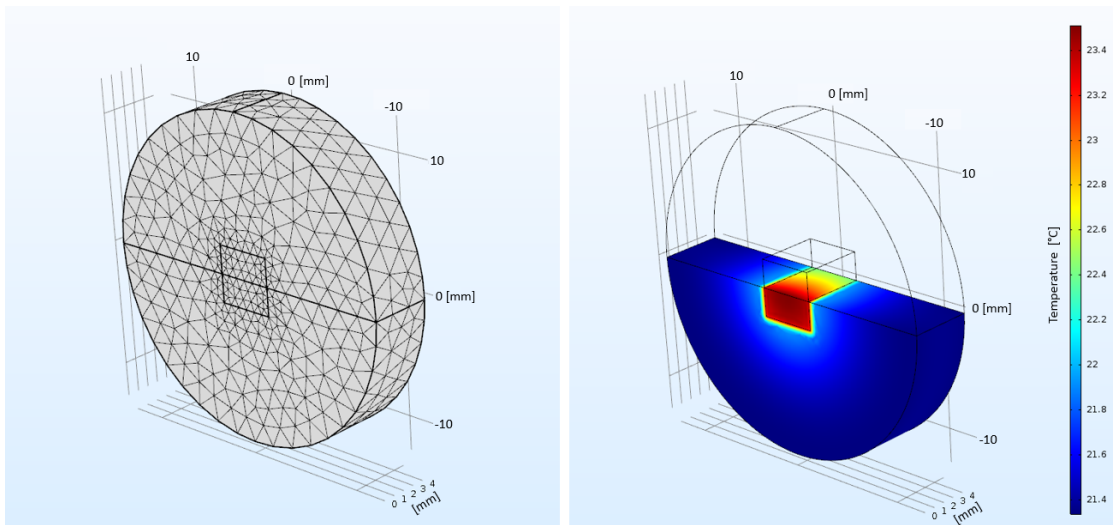

Figure 8: An example of the meshed Yb:YAG model (left) and a slice through the heated material surface (right) in COMSOL.

The results of the simulation can reveal the transformation of the temperature profile throughout the material with a high temporal and spatial resolution, but must be checked for validity using a thermal camera.

2.4 The Population Lens

The other type of pump-induced aberration present in this investigation is that of the so-called "Population Lens". The source of this effect stems from a difference in the "polarizability" of the dopant ion (Yb^{3+}) at the ground and excited states. The relationship between polarizability and the refractive index can be introduced through the use of basic EM-field theory and the Drude-Lorentz model.

Propagating electromagnetic (EM) radiation, such as that from a pump laser, exerts a vectorial force on a moving charge described by the Lorentz force:[15]

$$\vec{F} = q[\vec{E} + \vec{v} \times \vec{B}]. \tag{15}$$

The divergence and curl of the electric and magnetic fields are connected to their corresponding time derivatives (along with current and charge densities, if applicable). This coupled description of the electric and magnetic fields is shown using Maxwell's equations. An EM field interacting with a charged particle will cause the particle to accelerate, which then produces EM radiation that oscillates at a certain frequency. For a simple case, assume an oscillating EM field taking the form of a plane wave.[16] The electric field component E is described by

$$\vec{E} = E_0 e^{i(\vec{k}\cdot\vec{r}-\omega t)}, \tag{16}$$

with the physical quantity being the real part of equation 16. By inserting this ansatz into Maxwell's equations (given in the Fourier domain, denoted by "$\sim$")[16]

$$\nabla \times \tilde{\vec{E}} = i\omega\mu_0\tilde{\vec{H}}, \quad \nabla \times \tilde{\vec{H}} = -i\omega\tilde{\vec{P}} - i\omega\varepsilon_0\tilde{\vec{E}},$$

$$\nabla \cdot \tilde{\vec{D}} = -\nabla \cdot \tilde{\vec{P}}, \quad \nabla \cdot \tilde{\vec{H}} = 0, \tag{17}$$

a relationship is formed between the incoming EM field and the induced polarization:[16]

$$\Delta\tilde{\vec{E}} + \frac{\omega^2}{c^2}\tilde{\vec{E}} - \nabla(\nabla \cdot \tilde{\vec{E}}) = -\mu_0\omega^2\tilde{\vec{P}}. \tag{18}$$

H represents the magnetic field, P is the induced polarization, D is the dielectric displacement vector, ω is the frequency, c is the speed of light, ε_0 is the vacuum dielectric permittivity, and μ_0 is the vacuum magnetic permeability.

An atom can be described as a nucleus surrounded by a charge distribution, called an electron cloud. This electron cloud represents the orbit of the electrons around the nucleus. When an EM field interacts with an atom, the Lorentz force from the electric field (magnetic materials are not considered here) causes a separation of the charges, inducing a dipole moment. The shape of the electron cloud is distorted, and the electrons are accelerated. The restoring force in the medium (attraction between the nucleus and the electron cloud), given in the Drude-Lorentz model[15] as $m\omega_0{}^2 r$, attempts to pull the electron cloud back into the initial state, with an oscillation according to the material-dependent resonance frequency ω_0, the electron mass m, the charge q, and the displacement r of the electron cloud:

$$F = \left[\frac{\mathrm{d}^2}{\mathrm{d}t^2} + \gamma\frac{\mathrm{d}}{\mathrm{d}t} + \omega_0{}^2\right] m\vec{r} = q\vec{E}. \tag{19}$$

This is done by releasing energy in the form of EM radiation, with a frequency equivalent to the oscillating frequency of the induced dipole. The motion that induces the dipole moment $p = qr$ is dependent on the displacement of the electron cloud and the charge. On the macroscopic scale, the induced dipole moment multiplied by the dipole density N gives the polarization. The polarization $P = Np$ (in actuality, the polarization density) is therefore defined as the average induced displacement of the electron clouds of a medium due to an applied optical field. Rewriting equation 19 as

$$\left[\frac{\mathrm{d}^2}{\mathrm{d}t^2} + \gamma\frac{\mathrm{d}}{\mathrm{d}t} + \omega_0{}^2\right] \vec{P} = \frac{Nq^2}{m}\vec{E} \tag{20}$$

and solving for the induced polarization[15] (in the Fourier domain)

$$\vec{P}(\vec{r},\omega) = \varepsilon_0 \cdot \frac{\frac{Nq^2}{\varepsilon_0 m_e}}{\omega_0{}^2 - \omega^2 - i\gamma\omega} \cdot \vec{E}(\vec{r},\omega) = \varepsilon_0\chi(\omega)\vec{E}(\vec{r},\omega) \tag{21}$$

leads to an expression in terms of the susceptibility $\chi(\omega)$ of the dielectric material.

The EM field resulting from the polarization of the dielectric medium (through the induced dipole moments of the atoms), is not the same as the initial EM field. The EM field inside the medium (called the dielectric displacement field D)[16]

$$\vec{D}(\vec{r},\omega) = \varepsilon_0\vec{E}(\vec{r},\omega) + \vec{P}(\vec{r},\omega) \tag{22}$$

is a superposition of the initial EM field (the optical driver E) and the emitted EM field produced by the dipole moments (also called a "polarization wave", P, and is not to be confused with the polarization of the EM field itself, which describes

the direction of EM "oscillation"). Through the use of equation 21, the dielectric displacement field

$$\vec{\tilde{D}}(\vec{r}, \omega) = \varepsilon_0 \left(1 + \vec{\tilde{X}}(\omega)\right) \vec{\tilde{E}}(\vec{r}, \omega) = \varepsilon_0 \vec{\tilde{\varepsilon}}(\omega) \vec{\tilde{E}}(\vec{r}, \omega) \tag{23}$$

is formulated in terms of the dielectric permittivity $\varepsilon(\omega) = 1 + X(\omega)$ and the initial electric field.

Solving the wave equation (given in equation 18), through the use of equation 23 and the relationship $n(\omega) = \sqrt{\varepsilon(\omega)}$ between the refractive index and the dielectric permittivity, results in the dispersion relation[16]

$$\vec{k}(\omega) = \frac{\omega}{c}\vec{n}(\omega), \tag{24}$$

which shows that the propagation vector of the plane wave $k(\omega)$ is connected to the frequency of the wave ω and the refractive index $n(\omega)$ of the material. The end result, in the linear regime, is a reduction in the phase velocity of the initial field (shown through a change in the propagation vector), caused by the atoms with which the EM field is interacting. This reduction factor is the refractive index, which describes the combination of the incoming EM field and the induced polarization.

The ratio of induced dipole moments and applied electric field is called the polarizability α of an atom. In the cases relevant to this discussion, the polarizability is related to the susceptibility via[15]

$$\alpha = {}^{p}\!/_{E} = {}^{X}\!/_{N} = \frac{n^2 - 1}{N}. \tag{25}$$

The susceptibility X is not necessarily a scalar. For an anisotropic medium (which contains a certain atomic orientation), the electron cloud will distort differently in different directions, causing the polarization to vary with direction as well (this forces the X to be described as a tensor). In a linear regime, the polarizability states that as the amplitude of the electric field increases, the amplitude of each dipole moment increases by the same factor, as the electrons are driven harder. The polarizability increases with a higher number of electrons per volume (larger atoms) and with a larger separation between electrons and the nucleus, because the attractive force between the particles is weaker. Equation 25 also shows that a difference in the polarizability of a material directly translates into a change in the refractive index. Therefore, it is to be expected that a material doped with Yb^{3+}, which carries a polarizability difference at different excited states, will exhibit a different refractive index inside and outside the pumped regions, depending on the population in those states (ground level ${}^2F_{7/2}$ and upper lasing level ${}^2F_{5/2}$).

This results in an additional refractive index (phase-shift) profile that the material imbues onto the incident seed laser, much like a lens would, aptly justifying the name "Population Lens". The amplitude and shape of the refractive index profile is estimated using[22]

$$\Delta n_e = \frac{2\pi(n_0^2 + 2)}{3n_0}\Delta\alpha\Delta N, \tag{26}$$

with the knowledge of the level of population inversion ΔN within the material at a given time, the polarizability difference $\Delta\alpha$, and the unperturbed refractive index of the material n_0. The population lens, much like the thermal lens, is expected to relax after the pump has ended, but with a characteristic time near the lifetime of the excited-state (upper lasing level), since the population of that state decreases as the ions return to the ground state.

2.5   Phase Profile Extraction

The refractive index changes resulting from the pump-induced thermal and population lens effects can be measured with an interferometer. By forcing the superposition (interference) of two beams, at least one of which having passed through the pumped material, the phase imbued by the material onto the incident beam(s) will appear in the form of fringes (periodic light/dark patterns characteristic of interference), from which the desired information can be extracted. There are several conditions needed for interference to take place: similar intensities, compatible polarizations, temporal coherence, and spatial coherence. The strength of the interfering signals must be similar, otherwise the weaker signal and the fringe pattern will be hidden by the stronger signal. The polarization of the two interfering light waves must not be orthogonal, otherwise a fringe pattern will not form, since this pattern is dependent on the existence of a mixing (interference) term between the two waves. Take the following case of two superimposed waves with a phase difference ϕ and polarization directions e_1 and e_2 respectively:

$$E = E_1 cos(\omega t)\vec{e}_1 + E_2 cos(\omega t + \phi)\vec{e}_2. \tag{27}$$

Noting that the intensity of the resulting field is a value proportional to the cycle-averaged square of the electric field amplitude

$$I \propto \langle|E|^2\rangle = \langle|E_1|^2\rangle + \langle|E_2|^2\rangle + 2\langle|E_1 \cdot E_2|\rangle, \tag{28}$$

the general two-beam interference equation[16] (for monochromatic sources) can be formulated:

$$I = I_1 + I_2 + 2\sqrt{I_1 I_2}\,cos(\phi)(\vec{e}_1 \cdot \vec{e}_2). \tag{29}$$

For the case of orthogonal polarizations, the scalar product of the two electric field components is zero (since $\vec{e}_1 \perp \vec{e}_2 \Rightarrow \vec{e}_1 \cdot \vec{e}_2 = 0$), and thus the mixing (interference) term vanishes. For the case of two waves with parallel (or simply non-orthogonal) polarization directions, this mixing terms remains, which describes the fixed-phase relationship between the two waves, and from which the desired phase information can be extracted.

For a fringe pattern to occur, the coherence conditions must also be fulfilled, which quantifies the ability of electromagnetic radiation to spatiotemporally maintain a fixed-phase relationship. Temporal coherence is inversely related to the bandwidth $\Delta\lambda$ of a light source ($\tau_c \approx \frac{\lambda^2}{c \cdot \Delta\lambda}$), and can be mapped into a unit of length called the coherence length ($L_c = c \cdot \tau_c$). The optical path difference (OPD) between the two beams must be smaller than the coherence length, which is on the order of meters for monochromatic lasers and microns for ultrashort pulses. Spatial coherence is a measure of similarity (a cross-correlation) of positions on the wavefront profile. For largely-varying amplitudes across the wavefront, it should be expected that fringes will be difficult to observe, since the fixed-phase relationship may not be held for all positions when attempting to interfere two beams. A method to mitigate this issue is to install a spatial filter, in an effort to approximate a point source and cut off high spatial frequencies. After some distance away from the "point source", a relatively "flat" and even wavefront can be expected, due to the reduction in the original amplitude variations of the wavefront. When building an interferometric setup, it should be therefore noted that the visibility (contrast) of the fringes is maximized with the use of a single monochromatic, spatially-filtered laser source.

The fringe pattern signal can be described by a simplified version of the two-beam interference equation (equation 29), and is written here in complex form:

$$f = a + b \cdot cos(\phi) = a + \frac{b}{2}e^{i\phi} + \frac{b^*}{2}e^{-i\phi} = a + ce^{i\phi} + c^*e^{-i\phi}. \qquad (30)$$

By sending the signal into the Fourier domain (equation 31), the term C with the phase contribution can be separated from the signal, and an inverse Fourier transform can be computed to produce the desired phase component:[25]

$$\stackrel{\mathcal{F}}{\Rightarrow} F = A + C + C^* \xrightarrow[\mathcal{F}^{-1}]{\text{extract } C} c = \frac{b}{2}e^{i\phi} \Rightarrow \text{argument}(c) = \phi. \qquad (31)$$

This method can be utilized on an image containing a fringe pattern through the use of image manipulation tools, such as those within the development platform LabVIEW, in order to extract and analyze the pump-induced aberrations within the tested Yb^{3+}-doped active materials.

3 Pump-Induced Aberrations in Yb^{3+}-doped Active Materials

3.1 The Pump Engine

The goal of the investigation detailed in this thesis is to spatiotemporally characterize the phase-shift profiles resulting from the thermal and population lenses for the active materials used within the POLARIS laser system under similar pumping/cooling conditions. The first step in this process is to design and build a high power laser pump source, referred to as a "pump engine", with the aim of producing a uniform excitation of the active material.

3.1.1 Design Basics

For solid-state laser amplifiers, few types of sources remain viable when dealing with high powers. Laser diodes are semiconductors that can be built as single-emitters, or grown onto a bar, which consists of multiple single-emitters. When a high power output is required, many diode bars can be stacked together in a compact setup called a laser diode stack (LDS). The narrow emission spectrum and high radiance of a laser diode stack (as opposed to a flash lamp, which incoherently emits in a wide spectrum and over a wide angle) results in a stronger and more efficient absorption by the solid-state active material, which typically absorbs radiation in narrow bands.
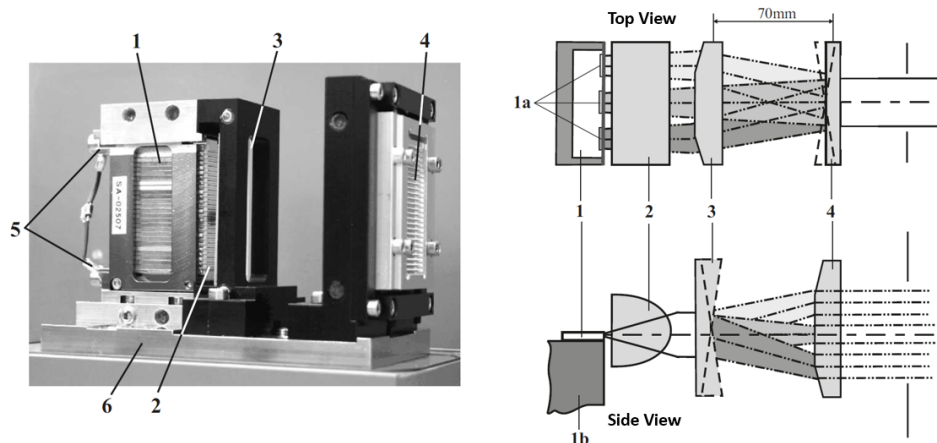

Figure 9: A laser diode stack (LDS) consisting of 25 laser diode bars (1) with an additional optical setup for beam compression.[17] The optical setup consists of fast-axis collimators (2), 3 prisms (3) which cut the 25 beams each into 3 parts, and 25 prisms (4) which redirect the Poynting vectors of the 75 beams to mimic the original. The electrical contacts shown in (5) are connected to a high-current driver. The system is water-cooled (6).

The pump engine, realized for the investigations detailed in this thesis, consists of two of the laser diode stacks shown in figure 9 as the pump sources, along with an additional optical system to homogenize the beam, since this source with 75 distinct (albeit closely spaced) laser lines does not exhibit a completely uniform pump profile.

The radiance, or brightness,[17] of a light source is a measure of the spatial and angular distribution of power, and is defined as:

$$L_{e,\Omega} = \frac{Power}{Area \cdot Solid\,Angle} = \left[\frac{\mathrm{W}}{\mathrm{cm^2 \cdot sr}} \right].$$

A large $L_{e,\Omega}$ value is representative of a laser beam with a high power concentrated into a tight profile in both spatial and angular dimensions. Radiance is a unique quantity which is invariant for any particular source, and thus, the radiance of a particular source cannot be improved through the use of an optical system (although in real systems, losses such as scattering or absorption can reduce the radiance). However, when a high radiance source is required, two polarized sources can be combined using a polarizing beamsplitter. The resulting radiance will be the combination of the radiance of the two sources along with some inevitable loss, stemming from material absorption/reflection and imperfect coupling/alignment. The LDS contains a fast axis (small aperture, high divergence; denoted FA) and a slow axis (large aperture, low divergence; denoted SA). The spatial distribution of the beam can be minimized through the use of telescopes for each axis. A Keplerian telescope is a set of two positive lenses which changes the magnification of an image, based on the ratio of the focal lengths of the lenses. This concept can be applied separately to the fast and slow axes of the laser beam by choosing cylindrical lenses. An optical system comprising of two telescopes can therefore force the initial beam (a rectangle of 75 lines) into a more spatially uniform pattern (i.e., a square of 75 lines). By combining two such beams together (oriented 90° with respect to each other), a square with a tight crosshatch pattern can be formed, which has an increased fill-factor when compared to the initial individual beams. Noting that, for typical laser diode stacks, the polarization of the electric field is oriented along the slow axis (along the width of each laser bar), the combination of the two initial beams can be accomplished via the use of a polarizing beamsplitter (in reverse), which merges orthogonal beams that carry orthogonal polarizations. Pump beam combination via polarization mixing techniques can only be applied to isotropic laser materials, for which pumping is polarization independent (which is not the case, e.g., for Ti:Sapphire, which is birefringent). The beamsplitter then feeds the combined beam into a microlens array (MLA) setup, which spatially redistributes the energy within the pump beam.
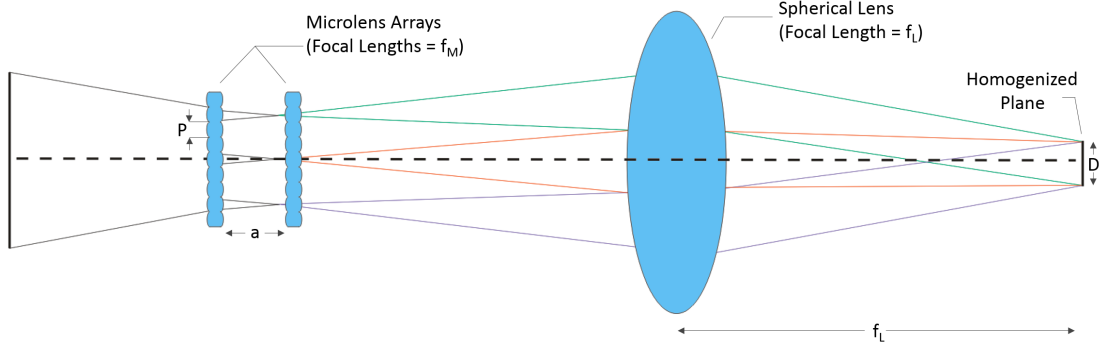
Figure 10: Microlens array setup: imaging fly's eye homogenizer. The beam diameter (D) in the homogenized plane is dependent on the distance between the MLAs (denoted a), the MLA pitch (P), the MLA focal lengths (f_M), and the focal length of the spherical lens (f_L).

The imaging fly's eye homogenizer,[18] shown in figure 10, consists of two MLAs and a spherical lens for imaging. The microlens arrays are rectangular glass plates (10 mm x 10 mm) formed from fused silica, which are etched to produce a pattern of miniature cylindrical lenses (pitch $\sim 250\,\mu$m), and afterwards AR-coated for the desired pump wavelength (940 nm). By placing two such MLAs in a crossed-configuration, the incoming beam will be split into multiple beamlets by the first MLA, and each beamlet will be imaged and superimposed onto the homogenized plane by the combination of the second MLA + the spherical lens. The MLAs are chosen to be identical (with a pitch $P = 250\,\mu$m), separated by a distance a $\approx f_M = \frac{R_C}{n-1} = \frac{0.75}{1.4512-1} = 1.66$ mm, and imaged by the spherical lens with a focal length $f_L = 100$ mm. The resulting beam diameter D of the homogenized pump source is estimated[18] by:

$$D = \frac{P \cdot f_L}{f_M^2} \left[2f_M - a \right] = P \cdot \frac{f_L}{f_M} = 1.5\,\text{cm}. \tag{32}$$

Although the list of key design considerations for forming a homogenized beam seems at first relatively short, an unwise choice of even the MLA pitch and separation distance can easily lead to detrimental effects. For a large pitch (pitch $> \frac{1}{3}$(input beam diameter)) and a low number of microlenses, the overlap will decrease, and thus the beam quickly becomes inhomogeneous. Placing the two MLAs closer than the focal length, such that the beamlet diameters are larger than the pitch of the second MLA, may cause crosstalk (overfilling) at the second MLA, leading to losses.

3.1.2   Optical Model

With the general idea of the pump engine design in place, constructing a simulation using FRED and performing a raytrace can shed light on some complexities in the design. FRED is an optical engineering software which allows the user to simulate light propagation through a multitude of optomechanical systems. FRED is compatible with many CAD softwares, and additionally provides the platform for constructing unique optical components. The program is a product of Photon Engineering, based in Tucson, AZ.

The first step in the simulation is to design the sources. The laser diode stacks are modeled in FRED as a coherent rectangular light source with a defined polarization (along the slow-axis), wavelength ($940\,\mathrm{nm}$), and power ($4.5\,\mathrm{kW}$). The next step is to apply a spatial reconstruction, in an effort to transform the rectangular profile into a square. This is done using two telescope sets, comprising of cylindrical lenses. The tight square pattern can be achieved with a slow-axis magnification of 2 and a fast-axis magnification of 0.15, based on the initial beam parameters (slow-axis: $3.7\,\mathrm{mm}$, fast-axis: $49\,\mathrm{mm}$). These magnification requirements directly translate into the focal length requirements for the cylindrical lenses (slow-axis: $100\,\mathrm{mm}:200\,\mathrm{mm}$, fast-axis: $250\,\mathrm{mm}:38\,\mathrm{mm}$). The dual-telescope setup is built in an overlaying fashion, as seen in figure 11, to conserve space ($100\,\mathrm{mm}:250\,\mathrm{mm}:200\,\mathrm{mm}:38\,\mathrm{mm}$), as long as the distances between the lenses in the slow-axis and fast-axis configurations, independently, remain fixed.
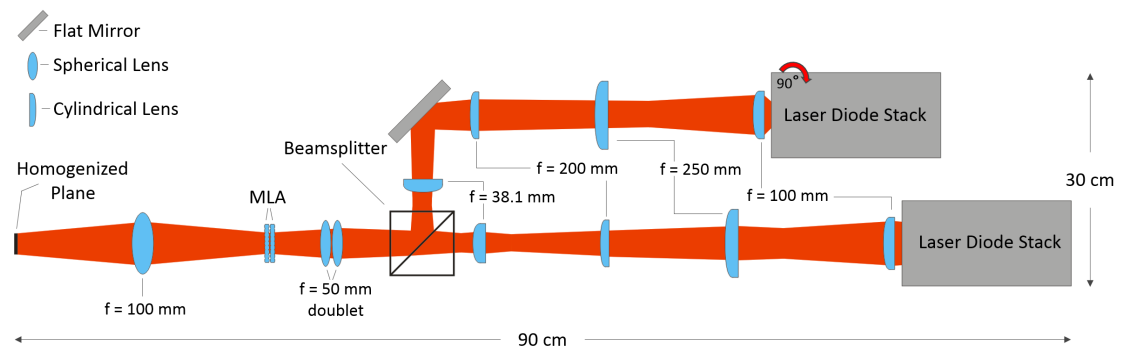

Figure 11: Illustrated setup of the optical model of the pump engine. The two laser beams, starting from the laser diode stacks, enter a dual-Keplerian telescope setup, followed by a beamsplitter, and finally the imaging fly's eye homogenizer. The homogenized plane, marked in the schematic, contains the desired beam size and profile.

The image plane for the two telescope systems must also be shared. Since an increased fill-factor is desired, the two beams, each with 75 tight lines, are combined with a polarization 90° with respect to each other, such that a cross-hatch pattern is formed. The resulting combined beam passes through a $50\,\mathrm{mm}$ effective

focal length doublet, which allows the beam to fit within the aperture of the imaging fly's eye homogenizer setup. This setup consists of two closely-spaced MLAs followed by a 100 mm focal length lens. According to the calculations performed earlier, this combination of optical components produces a homogeneous top-hat pattern with a beam width in both directions of 1.5 cm.

After building and inserting these components into the FRED software, a ray-trace is performed to ensure that all rays (excluding those lost due to absorption/reflection at the material surfaces or beamsplitter losses) arrive at the final image plane and produce the desired beam shape and size. An effort was made to improve the compactness of the system, by folding the outlying beamline with a mirror, since the entire pump engine should consume only a fraction of the space on the provided optical table.
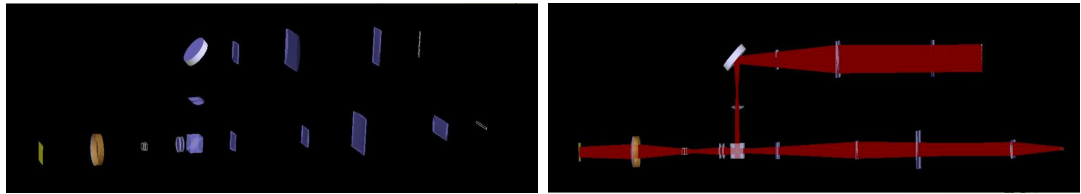

Figure 12: The FRED simulation process consists of an optical design (left) followed by raytrace (right).

A series of screenshots are displayed above in figure 12 and below in figure 13, which briefly illustrate the simulation and evaluation process. As desired, the simulation predicts a homogenized square beam carrying a width of 1.5 cm for both axes.
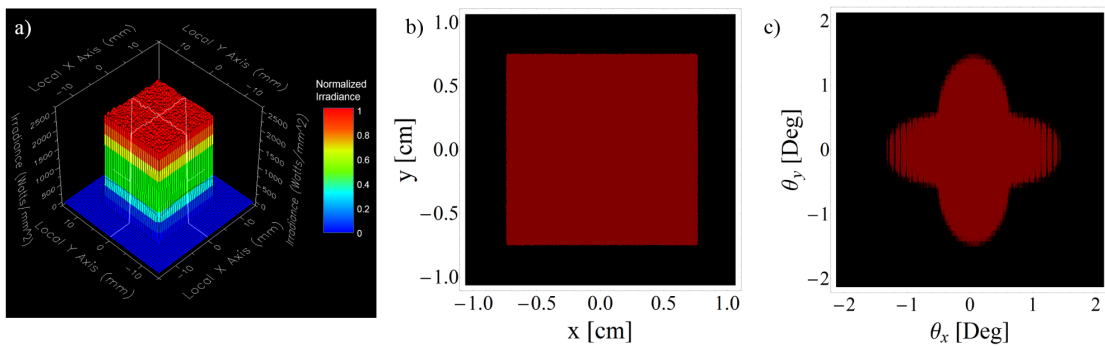

Figure 13: The FRED evaluation process resulted in a) a homogeneous irradiance profile with the desired beam shape and size in the b) near field and c) far field profiles. The focal spot pattern of the square-shaped near field profile is expected to be a crossed-superposition of two sinc functions, since the far field profile can be estimated from the Fourier transform of the near field profile.

3.1.3   Realization and Results

The measurements taken for the final system included scans, with respect to the current and pulse width settings on the given current driver, across the near field (spatial distribution), far field (angular distribution), energy (efficiency), and spectrum. The near field measurements displayed a square beam profile with a constant axis ratio of 1.06 throughout the entire current range of 20 A to 180 A. The far field measurements displayed a confinement of the beam's angular distribution, from a full divergence angle of 10.5° x 1° to 2.5° on both axes at maximum current. At 180 A and 1 ms pulse width, each laser diode stack was found to output at a power of 3.87 kW, while the final pump engine setup produced 6.8 kW, resulting in an 87% coupling efficiency between the two laser diode stacks and the complete optical system. The spectrum of the pump engine was centered at 936.8 nm, with a bandwidth of 3.6 nm. The radiance of the realized system, shown in figure 14, at maximum operating conditions is $1.15 \frac{\text{MW}}{\text{cm}^2 \cdot \text{sr}}$.

Figure 14: Final setup of the pump engine, equipped with a sealed "black box" cover (not shown) and handles for easy transport.

The near and far field scans, which produced the area and solid angle values for the calculation of the radiance, were averaged across the profile of a diffuser, which "captured" the image plane of the beam at the location of the diffuser. This step was necessary due to the high power of the pump sources, which would normally easily destroy the CCD within the camera while attempting to image the beam profile. The resulting near and far field profiles of the pump engine are displayed in figure 15.
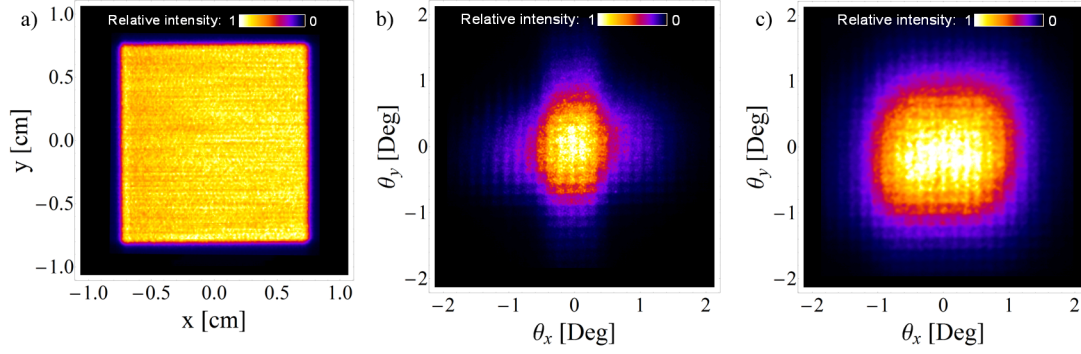
Figure 15: a) Near field (180 A) and far field (b) 20 A, c) 180 A) profiles of the pump engine. The horizontal line structure visible in a) is most likely a consequence of the measurement technique, which involves the imaging of a diffuser placed at the image plane corresponding to the near field profile. The diffuser is moved from side to side (in a horizontal line), and several images across the diffuser profile are averaged to produce the beam profile. This structure is not present in the pre-averaged images or when the pump beam profile on the surface of an active material is imaged. This line structure may exist as well in b) and c), since the same measurement technique was used, but is most likely overlaid by the strong mixing of the far field profile of the beam and the transfer (aperture) function of the MLAs (the focal plane of the beam is nearly incident to the surface of one of the MLAs, and thus, the structure of the MLAs are visible within the far-field).

With this homogeneous high radiance laser diode source, the investigated active materials can be pumped uniformly across the pump spot, such that the seed or measurement laser observes a similarly excited region of the material across its profile.

3.1.4   Pumping Configuration

The pumping configuration utilized throughout the investigation is depicted in figure 16. Each active material is pumped under normal incidence at the center of the material by the pump engine, with an empirically determined repetition rate according to the ability of the material to flush away heat (Yb:YAG - 2 Hz, Yb:CaF$_2$ - 4 Hz, Yb:FP15 - 0.2 Hz). Higher pump rates naturally resulted in stronger phase imprints, due to increased temperatures. The pump duration was chosen according to the upper lasing level lifetime: Yb:YAG - 0.9 ms,[32] Yb:CaF$_2$ - 2 ms,[32] Yb:FP15 - 1.4 ms.[17]
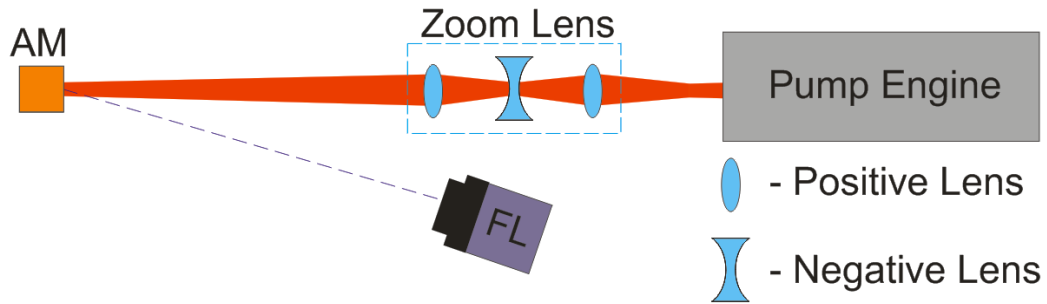
Figure 16: Illustrated setup of the pumping configuration. The pump laser passes from the pump engine, into a zoom lens setup, and onto the active material (AM). A FLIR (FL) thermal imaging camera is used to observe the change in temperature.

The material was pumped for several minutes before measurements were recorded, in order to approach a steady-state ("thermalized") regime in which the average temperature no longer increased with the number of cycles. This results in the observation of the thermal and population lens behavior in an equilibrium state during a periodic pump process, which occurs normally during use as an amplification medium.

3.2   Thermal Measurements vs. Simulation

Pumping the active materials results in an increase in temperature, and consequently a change in the refractive index. This temperature change can be simulated with COMSOL and tested for accuracy using a thermal camera. The in-house thermal imaging camera (FLIR P620) available for use is equipped with an uncooled microbolometer detector, which exhibits a strong a temperature-dependence of its resistance. An internal calibration process is used to convert the resistance of each pixel into a temperature value. Since each pixel requires a certain time (several ms) to heat up to the temperature of the image it is acquiring, frame rates faster than 30 fps have a higher chance to produce false temperature readings.[26] For this reason, the FLIR P620 camera was operated at 30 fps. Thermal cameras based on the cooled photon-counting detector exhibit a higher performance (integration time on the order of some μs), but are more costly, and unfortunately not available for this investigation. The internal calibration process of the thermal camera is dependent on the emissivity setting for the material, which gives the camera an understanding of how close the "emitted" radiation (from the surface/plane the camera is imaging) is to a perfect black body at the same temperature. The emissivity parameter ranges from 0 (mirror) to 1 (black body), and can be approximated by placing a piece of black tape on a material with a known temperature value, and adjusting the emissivity setting until

the measured temperature matches the known temperature. In this investigation, each material was placed in a water-cooled mount operating at nearly 21°C. The empirically determined emissivity value was 0.94. Thermal images of the pumped materials with the FLIR P620 camera are displayed in figure 17.
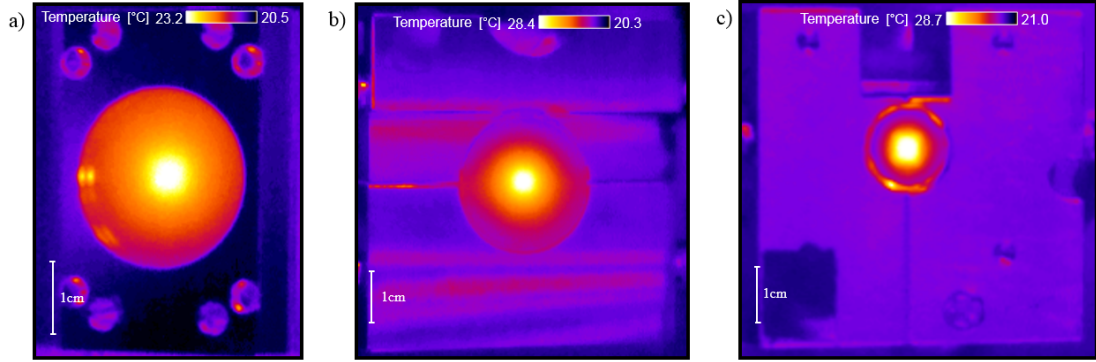

Figure 17: Thermal images (front) of the diode-pumped active materials: a) Yb:YAG (1 Hz), b) Yb:CaF$_2$ (4 Hz), and c)Yb:FP15 (0.2 Hz).

Due to the limitation of the slow detector, the COMSOL results could only be validated (seen in figure 18) every 33.3 ms with the thermal camera. A detection of the temperature spike per pump shot was only possible with Yb:FP15 due to the low thermal conductivity value. For Yb:YAG and Yb:CaF$_2$, the average simulated temperature profiles across the front and back of the materials were compared to the measured profiles, with a maximum temperature difference of less than 0.5°C. A slight asymmetry was present with the cooling by the Yb:FP15 mount, leading to a tilt ($\sim$0.3°C) in the measured temperature profiles. The temperature at the center of the pumped Yb:FP15 material was compared to the simulated results throughout the pump cycle, with a maximum temperature difference of less than 0.2°C.
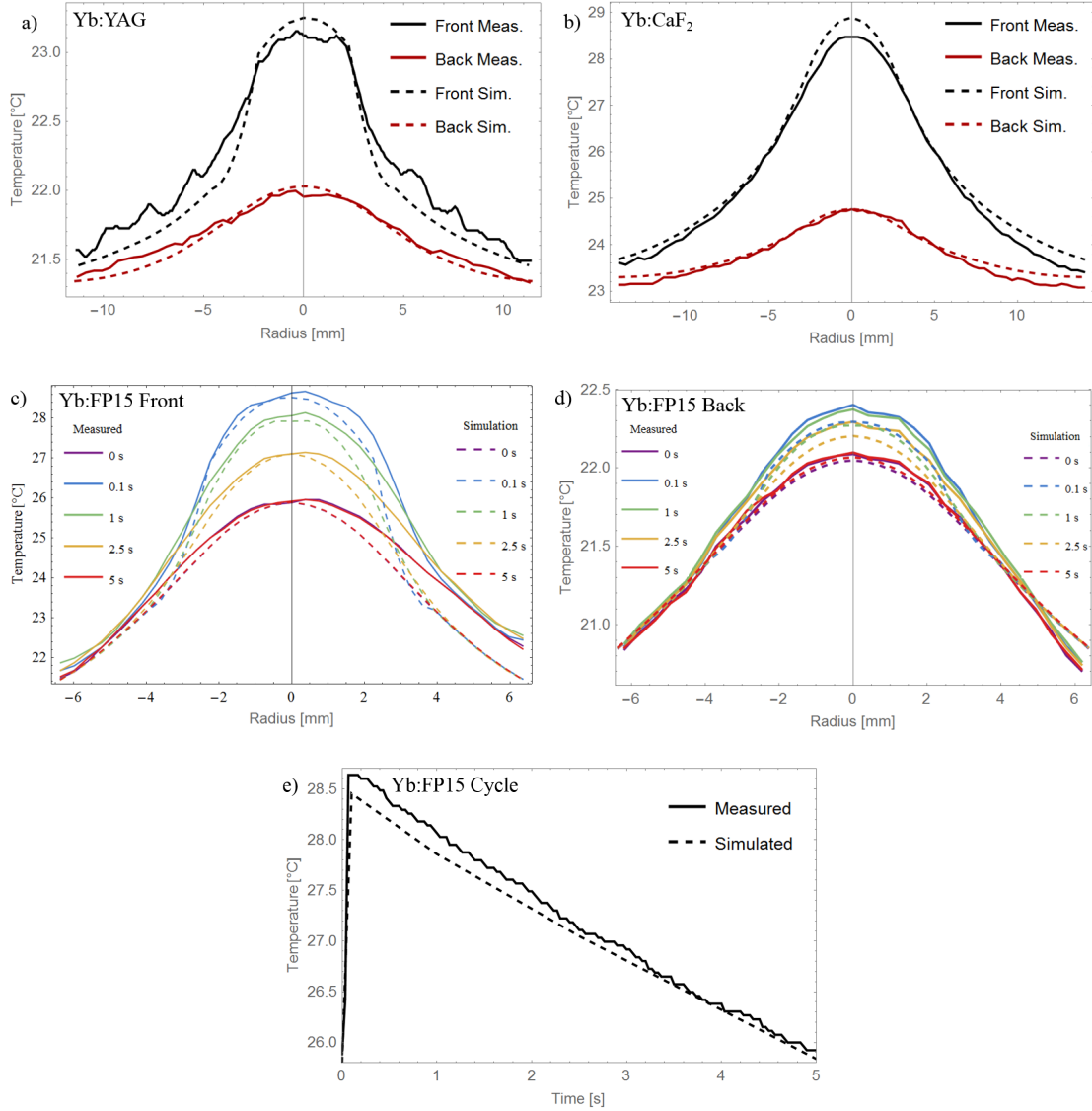
Figure 18: Comparison of measured (solid) and simulated (dashed) thermal profiles. Temperature changes within the pump cycle could not be resolved for a) Yb:YAG and b) Yb:CaF$_2$ due to the low temperature increase per pump spot and poor sensitivity of the FLIR camera. Instead, the measured temperature profiles on both the front and back of the crystals were compared to the simulated temperature profiles averaged over the pump cycle. The c) front and d) back Yb:FP15 profiles are displayed for times 0, 0.1, 1, 2.5, and 5 seconds within the pump cycle (rep. rate 0.2 Hz). e) The temperature in the center of Yb:FP15 is plotted throughout the pump cycle.

3.3   Experimental Setup for Phase-Shift Measurements

3.3.1   Testing Procedures

During the measurement process, the material is pumped from one side using the pump engine (1.5 cm beam width in both directions reduced to 4.5 mm by the zoom lens), as a spatially-filtered low power (5 mW) frequency-doubled Nd:YVO$_4$ continuous wave (CW) laser operating at 532 nm passes through the material from the other side at a minimized angle due to setup constraints. The CW laser, which acts as the light source for the interferometer (detailed in the following sections), is magnified from a 2 mm diameter to 33 mm using a simple telescope setup (30 : 500 mm focal lengths) to fill the entire cross-section of the material. The interference pattern produced from the interferometer was captured using a camera (Allied Vision, Manta G-032B) mounted with an objective, which was programmatically triggered through the use of a delay generator (Standford Research Systems, Model DG645) and LabVIEW. The spatial resolution of the measurement setup was 65 μm/pixel. The F/1.8 objective and 2x focal length extender, used in conjunction with the Manta CCD, is capable of imaging with a theoretical (diffraction) limit of 2.3 μm/pixel for the 532 nm wavelength measurement laser.

For each pump cycle, an image of the fringe pattern was captured at a single point in the cycle. The first image was recorded slightly before ($\sim$500 μs) the pump pulse arrived at the material. At the next designated pump cycle, the camera trigger was shifted such that an image was recorded directly at the pulse start. In this manner, images of the fringe patterns were captured throughout the entire cycle with a fine temporal resolution ($\sim$50 - 100 μs delays with an exposure time of 26 μs) within the pump period, and gradually decreasing temporal resolution (up to a time-shift in the second-regime for the Yb:FP15 case) after the pump ended. Each shot was repeated several times and an average of the phase profiles for each time stamp was implemented. From the analyzed data, two cases were explored. In the first case, in order to isolate the temporal properties of the refractive index changes that each pump shot induces within the material, the fringe pattern after thermalization (quasi-steady thermal state of the material) was utilized as the reference (background) data. For the spatial characterization, however, the full magnitude of the induced phase-shift profile throughout the entire pumping process is of importance. The reference data for this case is the fringe pattern before pumping. In order to sufficiently characterize the pump-induced refractive index changes in both a spatial and temporal sense, several interferometer setups were tested until a strong signal was obtained for all materials.

3.3.2   Plane-Plate Lateral Shearing Interferometer

The first attempt utilized the "Murty plane-plate lateral shearing interferometer", depicted in figure 19, which consists of a single glass window placed in the beam path at a non-zero angle of incidence.[23] Two Fresnel reflections occur due to the change in refractive index between air and glass on the front and back surfaces of the glass window. These two reflected beams are then superimposed with a slight spatial displacement (lateral shear) and interfere with each other. The OPD between the two beams is the refractive index of the glass window multiplied by its thickness, and is much smaller than the coherence length of the measurement laser.
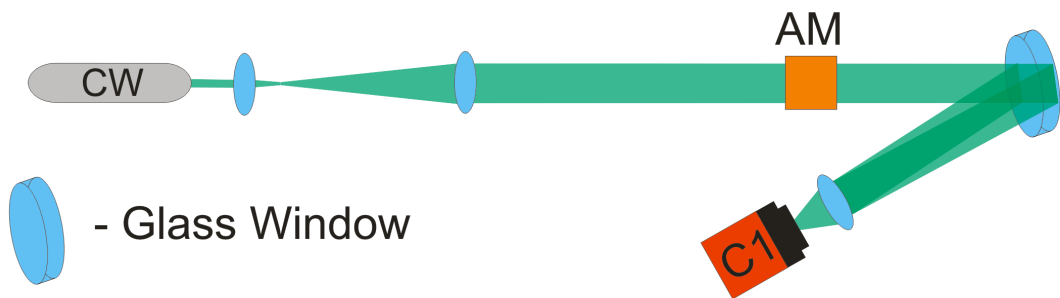

Figure 19: Illustrated setup of the plane-plate interferometer. The measurement beam (CW - continuous wave) passes through a telescope to fill the aperture of the active material (AM). The two Fresnel reflections from the glass window interfere and enter the camera (C1), which images the plane of the pumped active material.

The setup also offers the advantage of maintaining a single arm, such that both interfering beams travel through the exact same optical and ambient conditions, with the exception of the OPD caused by the glass window. In contrast, dual-arm interferometer setups may contain additional noise in the form of random fluctuations in the extracted phase profile, due to the heating of the air surrounding the pumped active material, through which only one of the interferometer beams propagates. The major trade-off for this simple interferometer setup is the lack of control of the fringe density, leading to difficulties in extracting only the phase term during the Fourier analysis. Due to the displacement (with a small distance Δx) of the beams with respect to each other, the fringe pattern observed does not directly grant the wavefront of the seed laser with induced "aberrations" by the thermal and population lenses in the material, but its derivative. Therefore, one must integrate the extracted phase in order to produce the desired results. The extracted phase, inseparable from the noise, was therefore integrated, yet only a minimal phase imprint was observed.

3.3.3 Air-Wedge Shearing Interferometer

The next interferometer design is referred to as the "Air-wedge shearing interferometer", which holds the benefit of a variable shear.[24] Building this setup (shown in figure 20) requires the replacement of the plane-parallel-plate with two closely-spaced glass wedges, from which four Fresnel reflections occur. Through the use of two tip-tilt mounts, the reflections from the back of the first wedge and the front of the second wedge can be directed into the objective-camera configuration, where the interference pattern can be observed. In this scenario, the OPD is on the order of some microns, and is also suitable for interference measurements with sources exhibiting small coherence lengths (i.e. short pulses).
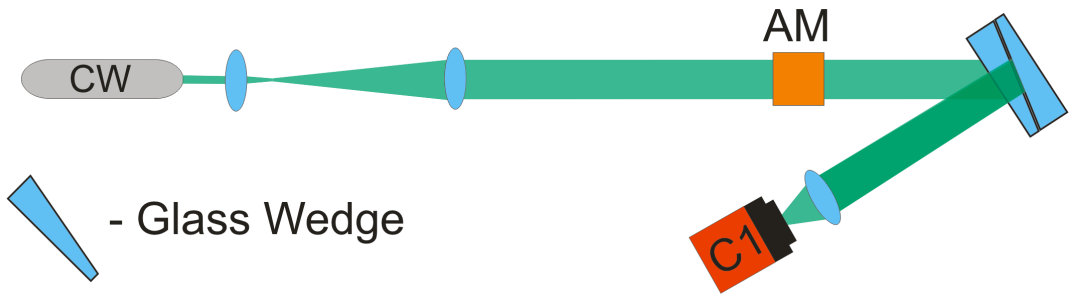

Figure 20: Illustrated setup of the air-wedge interferometer. The measurement beam (CW - continuous wave) passes through a telescope to fill the aperture of the active material (AM). The two Fresnel reflections from the air wedge interfere and enter the camera (C1), which images the plane of the pumped active material.

The ideal shear is formed from a trade-off between several rules. The intensity of the two beams can be increased by keeping the plane of the air gap between the wedges (nearly) orthogonal to the incident beam, since the Fresnel reflection coefficient is maximized at this angle. A higher fringe density can be coerced by increasing the angle between the two wedges, since the fringe spacing ($S = \frac{\lambda}{2n\theta}$) is inversely proportional to the air-wedge angle (θ). Increasing the fringe density (larger shear) results in a higher resolution during the phase extraction, but decreases the interference area. Through shearing, one inherently cuts off the side portions of each of the two beams, resulting in a loss of information (and therefore, the full phase-shift profile) at the material edges. Throughout multiple tests, phase signals were retrieved for the designated materials, but the integration of the noise component was the major limiting factor, leading to large fluctuations in what was expected to be a very smooth phase profile.

3.3.4   Mach-Zehnder Interferometer

The final interferometer design, depicted in figure 21, is a slightly modified version of the Mach-Zehnder interferometer, with the wedges from the previous setup employed instead of the typical beamsplitters. The Mach-Zehnder interferometer utilizes a double-arm configuration, in which the measurement laser is split into two components and later recombined. Interference fringes are produced when the beam passing through the arm containing the active material meets the beam passing through the reference arm (without the active material).
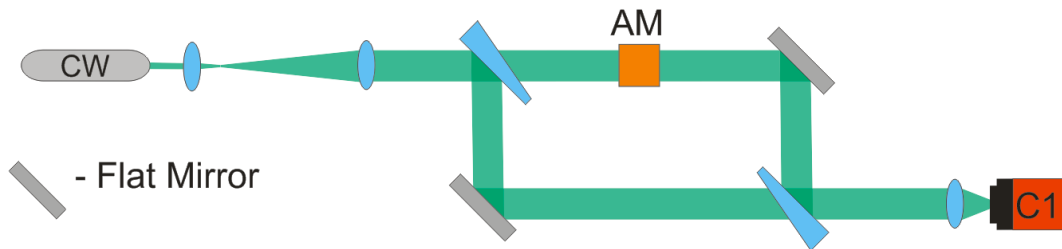

Figure 21: Illustrated setup of the Mach-Zehnder interferometer. The measurement beam (CW - continuous wave) passes through a telescope to fill the aperture of the active material (AM). The beam is split and recombined by two glass wedges, and the resulting interference pattern enters the camera (C1), which images the plane of the pumped active material.

Various tip-tilt mounts are used to control the direction and position of the beams. Since the concept of shearing interferometry is not utilized in this setup, processing the fringe patterns directly results in the phase-shift profile, not the derivative. A comparison of the fringe patterns from all interferometer setups can be seen in figure 22.
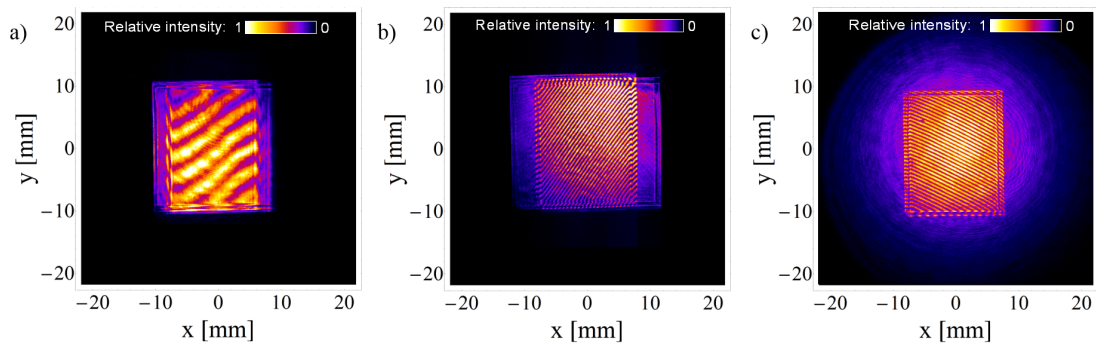

Figure 22: Comparison of fringe patterns from a Yb:CaF$_2$ sample produced by the a) plane-plate, b) air-wedge, and c) Mach-Zehnder interferometers. The Mach-Zehnder fringe pattern contains a similar number of fringes when compared to the air-wedge fringe pattern, yet without the loss of information on the material edges due to the shear or the requirement to integrate over the extracted phase signal (and noise).

During the alignment of the interferometer, the orientation of the fringes should be controlled to provide a separation of the amplitude (center component in figure 23b) and phase term (selected in green) in the Fourier domain, such that the phase term can be sufficiently extracted without carrying part of the amplitude term. This can be accomplished in real-time with a LabVIEW program which displays both the image of the interference pattern and its Fourier transform. As a rule of thumb, maintaining $7 \sim 10$ pixels per fringe yielded the optimum separation in the Fourier domain.
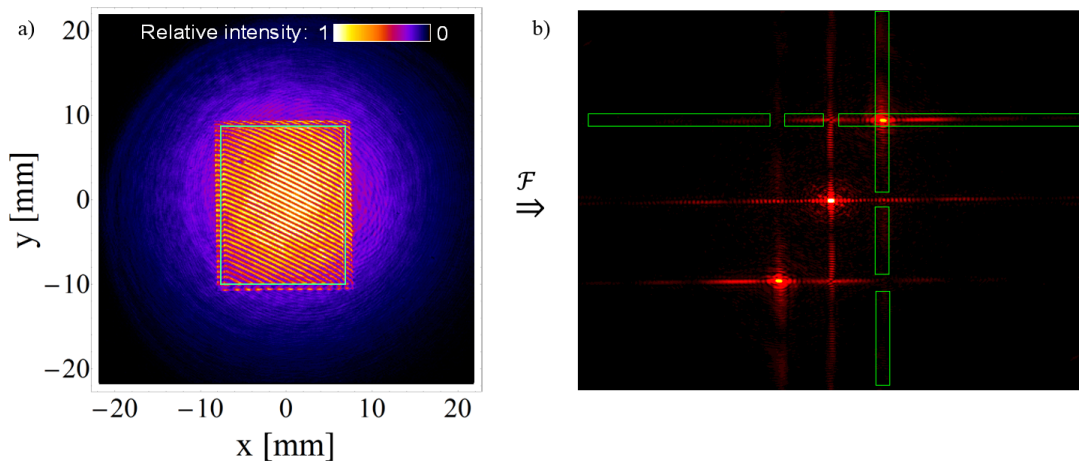

Figure 23: a) The fringe pattern must be initially extracted from the image using a specified "Region of Interest" (ROI). b) The selected image portion is then Fourier transformed and the fringe signal is mapped into spatial frequencies, in which a separation of the amplitude (center) and phase components (selected in green) can be observed. The gaps in the green area are purposefully omitted from the ROI in order to avoid processing certain portions of the amplitude and conjugate phase components that are mixed with the desired phase term.

The phase-contribution term (labeled "C" in equation 31) is isolated using an ROI, and only this component is inverse Fourier transformed. A high level of care must be taken when extracting the correct frequencies (corresponding to the phase component) in order to remove noise, yet retain a sufficient amount of phase information. An ROI which is too large in the Fourier domain results in a noisy, yet sharp phase profile, while a small ROI results in a smooth, blurry phase profile. Extracting the argument of the inverse Fourier transform of the phase-contribution term ("C", contained within the ROI) produces an array of wrapped phases. Since the interference pattern is periodic, the phase must be "unwrapped", which requires the connection of each discontinuity at intervals of 2π. A line-out of the unwrapped phase results in the desired phase-shift profile. The measurement setup and analysis software were calibrated by comparing the theoretical and measured phase profiles of both a positive and negative long focal

length ($>2\,$m) lens.

The fringe patterns at the beginning and end of the pump pulse are shown in figure 24 for the case of Yb:YAG, along with the corresponding unwrapped phases acquired through the LabVIEW fringe analysis program. The analysis reveals the imprint of the pump profile on the phase of the measurement laser by the pumped active material. The unwrapped phases for Yb:CaF$_2$ and Yb:FP15 at the end of the pump pulse are also displayed. The Yb:CaF$_2$ sample shown previously was replaced with a larger and thicker sample for the final tests.
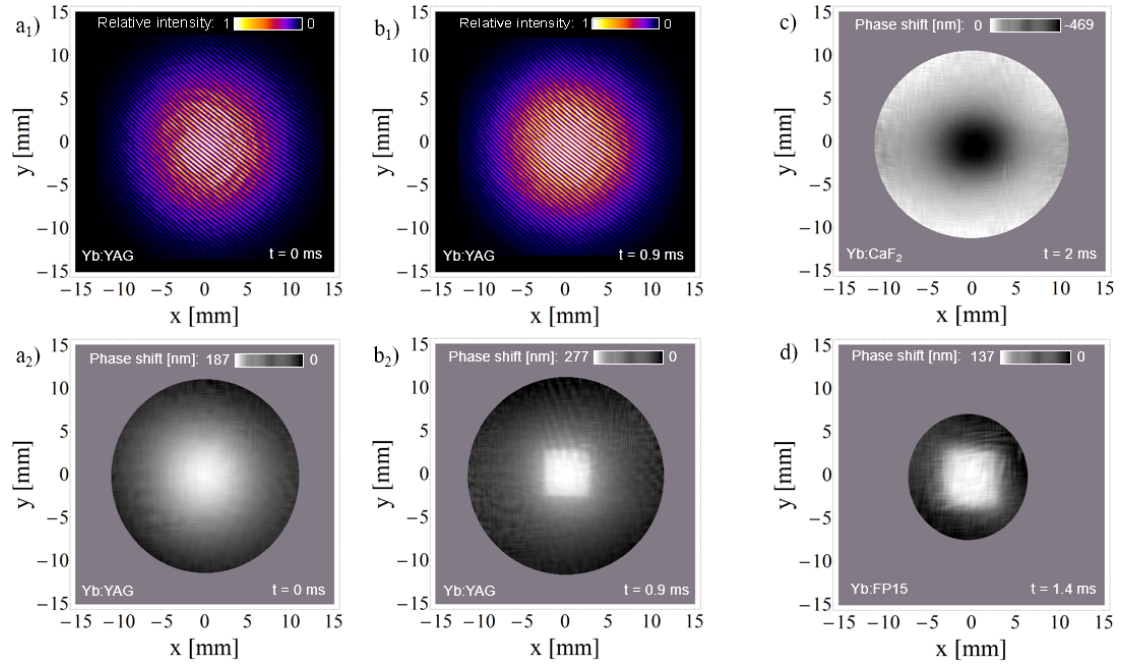

Figure 24: Comparison of fringe patterns (a_1, b_1) and unwrapped phases (a_2, b_2) for the case of Yb:YAG. The times denoted 't = 0 ms' and 't = 0.9 ms' refer to the start and end of the pump pulse respectively. Measurements were recorded after the materials have reached a quasi-steady temperature state, leading to a non-zero phase profile at the start of each pump shot ('t = 0 ms'). The differences between the direct fringe patterns seem only slightly visible with the human eye, yet reveal significant changes in the unwrapped phase within the 0.9 ms pump shot. The unwrapped phases for c) Yb:CaF$_2$, and d) Yb:FP15 at the end of the pump pulse are also displayed here.

A line-out through the center of each phase profile is extracted and saved for data compilation through another LabVIEW program. This process is repeated automatically for each measured period in time during the pump cycle. The full spatiotemporal characterization of the phase-shift profile can be observed through the analysis of the resulting data set.

3.3.5   Measured Phase-Shift Profiles

By extracting the phase-shift profiles for each material at different times in the pump cycle, comparisons between the materials can be constructed. The plots in figure 25 depict the total accumulated phase from the beginning of the pumping process until after thermalization (equilibrium), and reveal sharp phase-shifts (ϕ) within the pump beam width (4.5 mm) for each material, with a rise in phase during the pump shot (Yb:YAG: 0 - 0.9 ms, Yb:CaF$_2$: 0 - 2 ms, Yb:FP15: 0 - 1.4 ms) and a subsequent relaxation thereafter (Yb:YAG: 0.9 ms - 0.5 s, Yb:CaF$_2$: 2 ms - 0.25 s, Yb:FP15: 1.4 ms - 5 s). The measurements also show that Yb:YAG and Yb:FP15 cause an increased delay (positive ϕ) in the center of the beam, leading to a positive lens effect, while Yb:CaF$_2$ (negative ϕ) results in a strong negative lens.
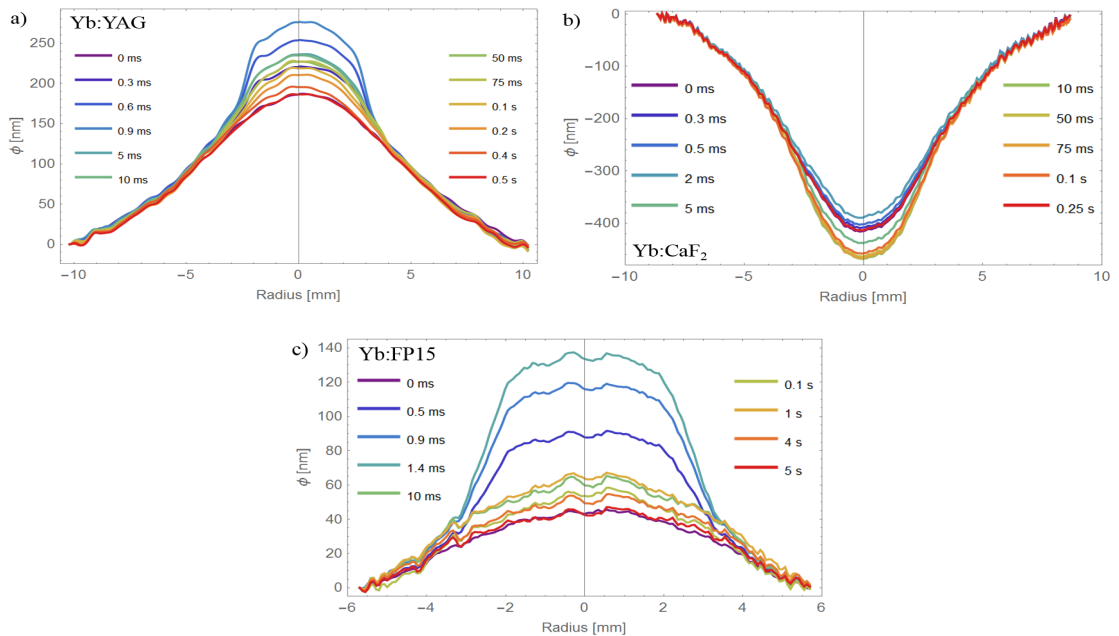

Figure 25: Selected phase-shift profiles measured by the Mach-Zehnder interferometer: a) The positive phase-shift (resembling a positive lens) exhibited by Yb:YAG increases in magnitude from the beginning of the pump cycle (0 s) until the end of the pump pulse (0.9 ms), after which a relaxation begins until the end of the pump cycle (0.5 s). The same positive progression can be seen for b) Yb:CaF$_2$ (negative lens, phase-shift increases / becomes more positive from 0 - 2 ms, relaxation from 2 ms - 0.25 s) and c) Yb:FP15 (positive lens, increase from 0 - 1.4 ms, relaxation from 1.4 ms - 5 s).

A further understanding of the temporal behavior of the aberrations induced by each pump pulse can be gained by plotting the change in the phase-shift profile throughout the pump cycle. For this case, the thermalized state was taken as the reference. The values shown in figure 26 represent the phase-shift averaged over the pumped region (4.5 mm), since the effect of the complete homogenized pump profile (as opposed to simply the center point of the pump) is desired for

this investigation. In addition to the positive increase in the phase-shift during the pump pulse and the subsequent relaxation thereafter, competing effects seem to be present for the Yb:CaF$_2$ and Yb:FP15 cases.
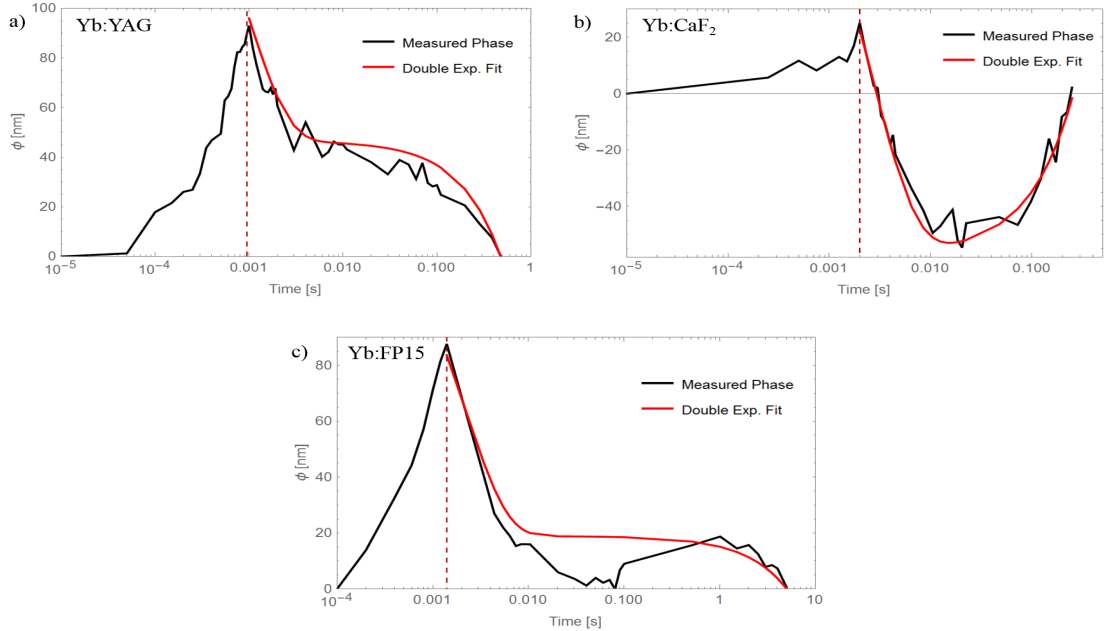

Figure 26: Measured temporal behavior of the phase-shift profiles induced by each pump pulse for a) Yb:YAG, b) Yb:CaF$_2$, and c) Yb:FP15. The results are plotted on a logarithmic time scale to more adequately reveal the progression of the phase-shifts across both the millisecond and second regime. As observed earlier with the spatial characterization, the temporal profile indeed shows a rise until the end of the pump pulse (dashed red line), followed by a general relaxation until the end of the pump cycle (the inverse of the repetition rate). The results from the Yb:CaF$_2$ and Yb:FP15 measurements seem to depict a competition between two opposing effects. The Yb:FP15 case deviates within a certain time frame from the double exponential curve fit, which was applied to each data set. The phase-shift (initially calculated in radians) is converted to units of nanometers according the wavelength (532 nm) of the measurement laser used in the interferometer setup.

A further characterization of the relaxation of the phase-shifts were performed by constructing a (double exponential) curve fit of the data, the results of which will be detailed in section 3.5.

3.4   Predicting the Pump-Induced Phase-Shift

With the knowledge of the total pump-induced phase-shift profile, the remaining investigation seeks to determine if this effect is truly a superposition of the thermal and population lenses. In order to accomplish this, the thermal and population lenses must be accounted for separately, in both a spatial and temporal sense.

3.4.1 Thermal Lens Characterization

Through the use of equation 12, the phase-shift can be calculated from the simulated temperature profiles. In a similar manner to the results from the Mach-Zehnder measurements, the spatial and temporal phase-shift profiles are plotted in figures 27 and 28.
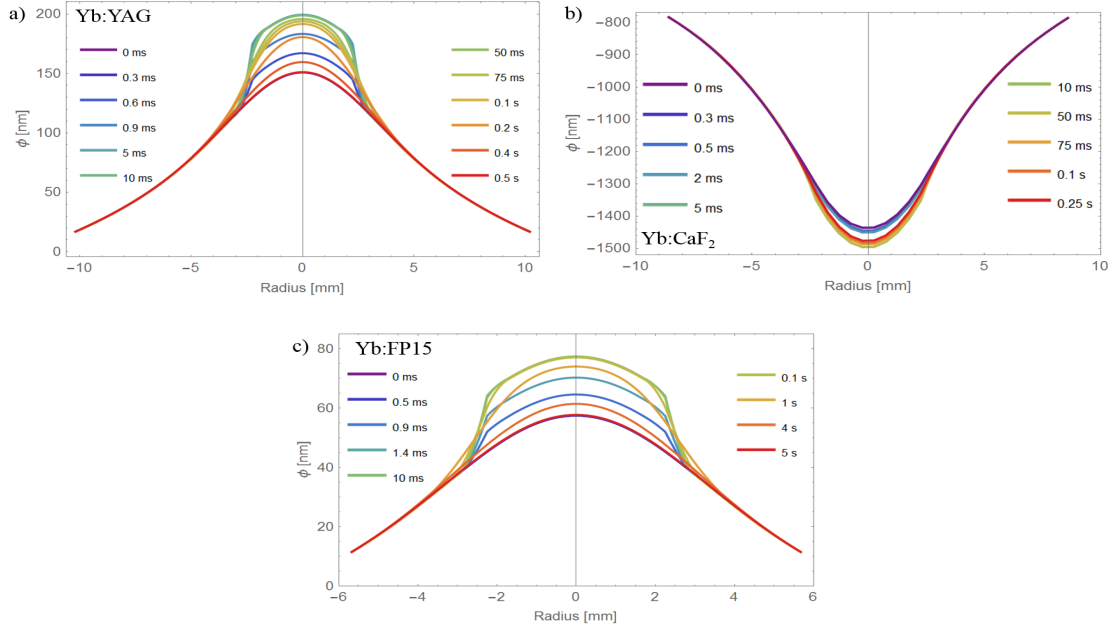

Figure 27: Simulated thermal lens spatial profiles for a) Yb:YAG, b) Yb:CaF$_2$, and c) Yb:FP15, displayed at times equivalent to those of the phase measurements in figure 25. The phase-shift at the edges of the materials is non-zero due to a temperature offset from the initial (room) temperature, since the heat transfer coefficient of the water-cooled thermal contact surrounding the mounted active materials is low. This offset is particularly large for the Yb:CaF$_2$ case, and thus, as a mere visual aid, the x-axis of the plot was shifted vertically.

Figures 27 and 28 show that the thermal lens for Yb:YAG and Yb:FP15 are initially positive, and become more positive during the pump shot, after which this effect relaxes until the next pump cycle begins. Yb:CaF$_2$ exhibits the analogous case, except with a negative thermal lens. Although in the measured phase (Mach-Zehnder) results for Yb:CaF$_2$, the phase-shift became more positive during the pump pulse, the phase-shift here becomes more negative (increases in magnitude). The non-zero baseline for the phase-shift profiles in figure 27 is caused by a difference in temperature from the initial (pre-pumping) temperature at the edges of the material. If the material were allowed to cool completely towards room temperature (no more pump pulses), the relaxation would follow an exponential form, with a time constant dependent on the specific heat capacity (which controls the temporal temperature change, as shown in equation 13), material density, and thermal conductivity.
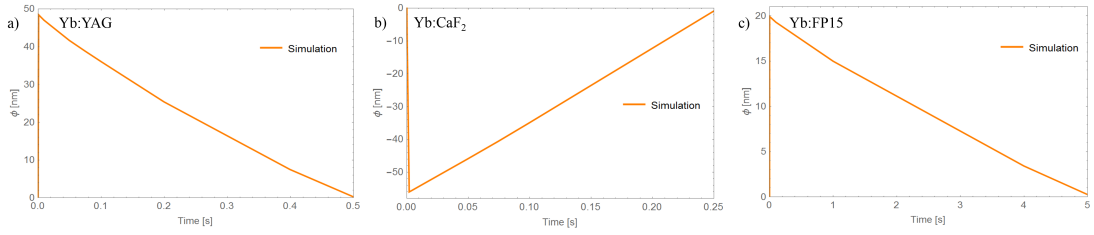
Figure 28: Simulated shot-to-shot temporal behavior of the thermal lens for a) Yb:YAG, b) Yb:CaF$_2$, and c) Yb:FP15. The temperature profile (and thus, the thermal lens) induced by each pump pulse returns to the thermalized state after the pump period has ended (according to the inverse of the repetition rate: a) 0.5 s, b) 0.25 s, and c) 5 s). The phase-shift (initially calculated in radians) is converted to units of nanometers according the wavelength (532 nm) of the measurement laser used in the interferometer setup.

3.4.2   Population Lens Characterization

The temporal behavior of the population lens can be ascertained with the knowledge of the level of inversion ΔN and the polarizability difference $\Delta \alpha$ of the material, as described in equation 26. The temporal profile of the population inversion level throughout the pump cycle can be extracted from single-pass gain measurements with the active materials. The measurement beam in this setup, shown in figure 29, was a 50 mW, 2.2 mm ($1/e^2$ diameter, TEM$_{00}$-mode), 1030 nm (fine-tunable) wavelength CW laser. The beam was centered within the pump spot (4.5 mm width) in the active material.

Figure 29: Illustrated setup of the gain measurement configuration. The pump laser passes from the pump engine, into a zoom lens setup, and onto the active material (AM). The measurement beam (CW - continuous wave) passes through the pumped active material and into a Thorlabs DET36A/M photodetector (PD) connected to an oscilloscope, which measures the signal strength throughout the pump cycle. A camera (C2) is used to image the plane of the pumped active material, in order to ensure proper CW/pump overlap and to capture the spatial fluorescence profile.

The wavelength of the laser for this setup must be precisely set to 1030 nm due the strongly wavelength-dependent emission cross-section of the active materials. For this reason, a pick-off mirror was installed in the setup which can be raised to send the CW laser into a spectrometer, located near the camera used for the Mach-Zehnder interferometer. A camera was placed facing the back side of the material to observe the integrated spatial profile of the fluorescence light, which is expected to match the spatial profile of the population lens. At the end of the pump pulse, the single-pass gain value for each active material was determined

to be: 1.4 for Yb:YAG (0.9 ms pump duration), 1.15 for Yb:CaF$_2$ (2 ms pump duration), and 1.2 for Yb:FP15 (1.4 ms pump duration). Through the utilization of equation 11, the level of population inversion in the material throughout the pump cycle could be extracted. It can be expected that the maximum inversion is populated (along with a maximum magnitude of the population lens) at the end of the pump pulse, followed by an exponential decay as the stored energy is released through the stimulated or spontaneous emission processes. The calculation of the refractive index change in the material, using the temporal profile of the population inversion, can be translated into a (spatio-)temporal OPD that the incident wavefront experiences. The results of the temporal profile of the phase-shift due to the population lens for each material is shown in figure 30.
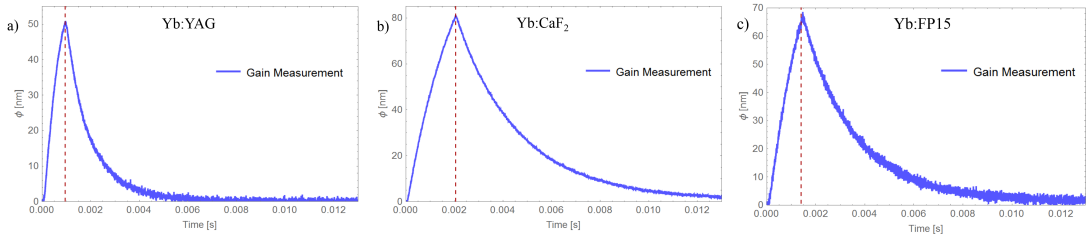

Figure 30: Temporal behavior of the population lens induced by each pump pulse. The phase-shift increases until the end of the pump pulse (dashed red), after which a fast exponential relaxation occurs (millisecond regime) with a time constant on the order of the fluorescence lifetime. The phase-shift (initially calculated in radians) is converted to units of nanometers according the wavelength (1030 nm) of the seed laser used in the gain measurement setup.

The gain measurements (population lens) and interference measurements (total pump-induced phase-shift) utilized CW lasers of different wavelengths: 1030 nm and 532 nm, respectively. Since the emission spectra of the active materials have high values at 1030 nm, a strong lasing (stimulated emission) process is initiated with the use of a seed laser at this wavelength. This is ideal for gain measurements, but the influence of this additional lasing process cannot be separated from the desired information from the interference measurements. The goal of this investigation is to measure the refractive index changes associated with the pumping process of the active materials present in the POLARIS laser system, and thus any constant offset of the refractive index value (according to the Drude-Lorentz model, an absorption or emission peak at a given wavelength results in a refractive index offset) caused by the seed laser is mostly removed by subtracting a set reference from the results of the interferometer measurements. A slight offset of the total accumulated phase may be present with a change in the wavelength of the seed laser, but the underlying physics remains unperturbed.

3.5   Comparison of Predicted and Measured Pump-Induced Aberrations

With the knowledge of the temporal profiles of the thermal and population lenses for the three Yb^{3+}-doped active materials, a superposition of the two effects is constructed and displayed in figure 31. For each pump shot, the induced population lens compared to the induced thermal lens is similar in both sign and magnitude for Yb:YAG. For the Yb:CaF$_2$ case, the two effects are similar in magnitude but are competing (opposite in sign). No competition is observable for Yb:FP15, as the signs of both lens effects are positive, although the population lens is stronger than the thermal lens (induced by a single shot) by roughly a factor of three.
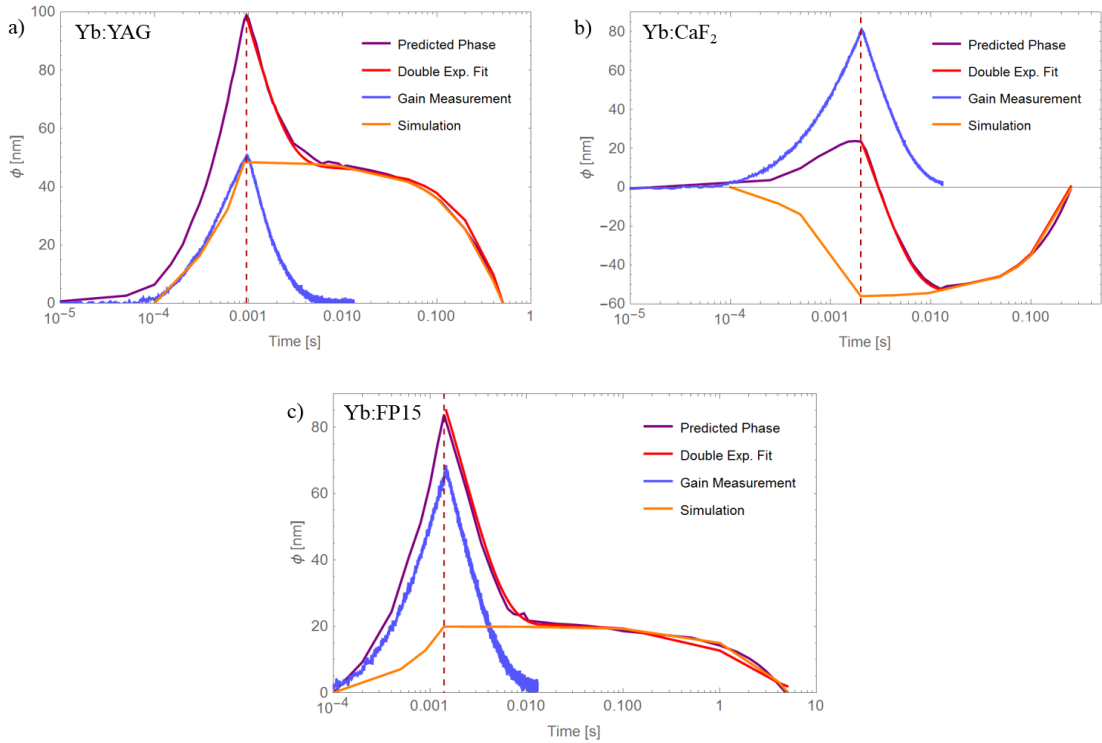

Figure 31: Temporal superposition of the thermal and population lenses for each tested active material, displayed in a logarithmic time scale to emphasize the pumping and relaxation regimes. The previously discussed "competing effects" between the population and thermal lenses for the Yb:CaF$_2$ case are revealed here. The values along the independent axis represent the change of the phase-shift from the accumulated value (at the thermalized state) during the entire length of the pump cycle (the inverse of the repetition rate). The end of the pump pulse is marked by the dashed red line.

The goal of this investigation is to observe whether the superposition (in purple) of the thermal and population lens effects are equivalent to the phase changes measured with the interferometer (in black), in an effort to reveal that the pump-induced phase-shifts can be predicted with merely single-pass gain (and corresponding fluorescence profile) measurements, and a temperature profile simulation

45

(or measurements with a thermal imaging camera exhibiting a temporal resolution finer than the pump duration). The similarities between the measured and predicted phase-shifts are shown in figure 32.
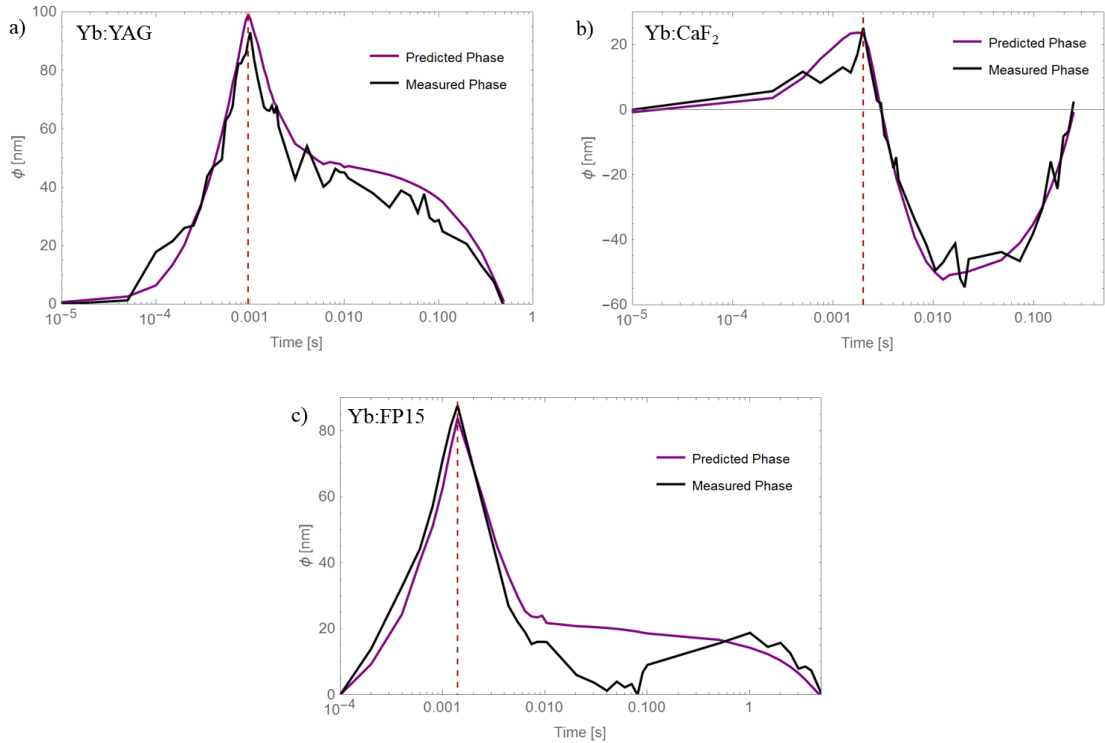

Figure 32: Temporal comparison of the measured results with the predicted superposition of the thermal and population lenses induced by each pump pulse. The end of the pump pulse is marked by the dashed red line, at which point the relaxation of the phase-shift begins.

In order to achieve a more tangible comparison, a temporal function of the phase-shift profiles has been constructed as a combination of the exponential relaxations of the thermal (denoted with subscript "th") and population (denoted with subscript "e", since it is an electronic aberration) lenses:

$$\phi_{relax}(t) = A_e \cdot e^{\frac{-t}{\tau_e}} + A_{th} \cdot e^{\frac{-t}{\tau_{th}}}. \tag{33}$$

By fitting this double exponential function to the measured and predicted phase-shifts, the amplitudes and time constants of the pump-induced aberrations can be extracted.

Tables 2-4 compare the amplitudes and time constants of the measured (interferometer) and "predicted" (simulation + gain measurement) pump-induced aberrations for each tested material. The amplitudes A_{th} and A_e correspond to the magnitudes of the phase-shift from the thermal and populations lenses generated from each pump pulse. It is found that the time constant from the population lens τ_e (Yb:YAG: $0.99\,\mathrm{ms}$, Yb:CaF$_2$: $2.74\,\mathrm{ms}$, Yb:FP15: $2.23\,\mathrm{ms}$) is on the order of

46

the fluorescence lifetime τ_{fl} (Yb:YAG: 0.9 ms, Yb:CaF$_2$: 2 ms, Yb:FP15: 1.4 ms). The population lens lifetime is longer than the fluorescence lifetime due to reabsorption over the material length. The time constant from the thermal lens τ_{th} (Yb:YAG: 0.48 s, Yb:CaF$_2$: 0.25 s, Yb:FP15: 5.02 s) closely resembles the thermal diffusion time τ_D (Yb:YAG: 0.4 s, Yb:CaF$_2$: 0.35 s, Yb:FP15: 4.73 s), which is taken as an approximate measure of the thermal relaxation.

Table 2: Relaxation function parameters for the measured (meas.) and predicted (pred.) pump-induced aberrations for Yb:YAG. The "given" values τ_e and τ_{th} correspond to τ_{fl} and τ_D respectively.

Yb:YAG	τ_e [ms]	A_e [nm]	τ_{th} [s]	A_{th} [nm]	$\Delta\alpha$[22] [10^{-26} cm^3]
Given	0.9	–	0.4	–	1.95±0.8
Meas.	0.99	49.49	0.48	46.47	–
Pred.	1.03	50.50	0.5	47.11	1.95

Table 3: Relaxation function parameters for the measured (meas.) and predicted (pred.) pump-induced aberrations for Yb:CaF$_2$. The "given" values τ_e and τ_{th} correspond to τ_{fl} and τ_D respectively.

Yb:CaF$_2$	τ_e [ms]	A_e [nm]	τ_{th} [s]	A_{th} [nm]	$\Delta\alpha$ [10^{-26} cm^3]
Given	2	–	0.35	–	–
Meas.	2.74	79.27	0.25	-56.52	–
Pred.	2.73	79.24	0.25	-56.69	0.96

Table 4: Relaxation function parameters for the measured (meas.) and predicted (pred.) pump-induced aberrations for Yb:FP15. The "given" values τ_e and τ_{th} correspond to τ_{fl} and τ_D respectively.

Yb:FP15	τ_e [ms]	A_e [nm]	τ_{th} [s]	A_{th} [nm]	$\Delta\alpha$[30] [10^{-26} cm^3]
Given	1.4	–	4.73	–	2.3±0.7
Meas.	2.23	64.78	5.02	18.87	–
Pred.	2.30	64.87	4.95	19.62	2.2

The comparability of the measured and predicted results is given with R^2 values above 0.9 for all results, with the exception of the measured (Mach-Zehnder) phase-shift for Yb:FP15. This is due to an additional artifact observed in the measurements (seen in figure 32c) that results in an R^2 value near 0.75 for the curve fit, and will be addressed towards the end of this section. Present with the other values in table 3 is the calculated polarizability difference $\Delta\alpha$ of the Yb^{3+}

ions within the CaF_2 host material, which is comparable to the other materials when considering the uncertainties (Yb:YAG $\sim \pm 40\,\%$, Yb:FP15 $\sim \pm 30\,\%$) in the given values. This is, to the best of my knowledge, the first time this value has been presented for this active material commonly used in diode-pumping schemes. The RMS displacement between the predicted and measured temporal phase-shift in figure 32 is nearly $5\,\text{nm}$ for each tested material (Yb:YAG - 5.34 nm, Yb:CaF_2 - 4.75 nm, Yb:FP15 - 6.87 nm).
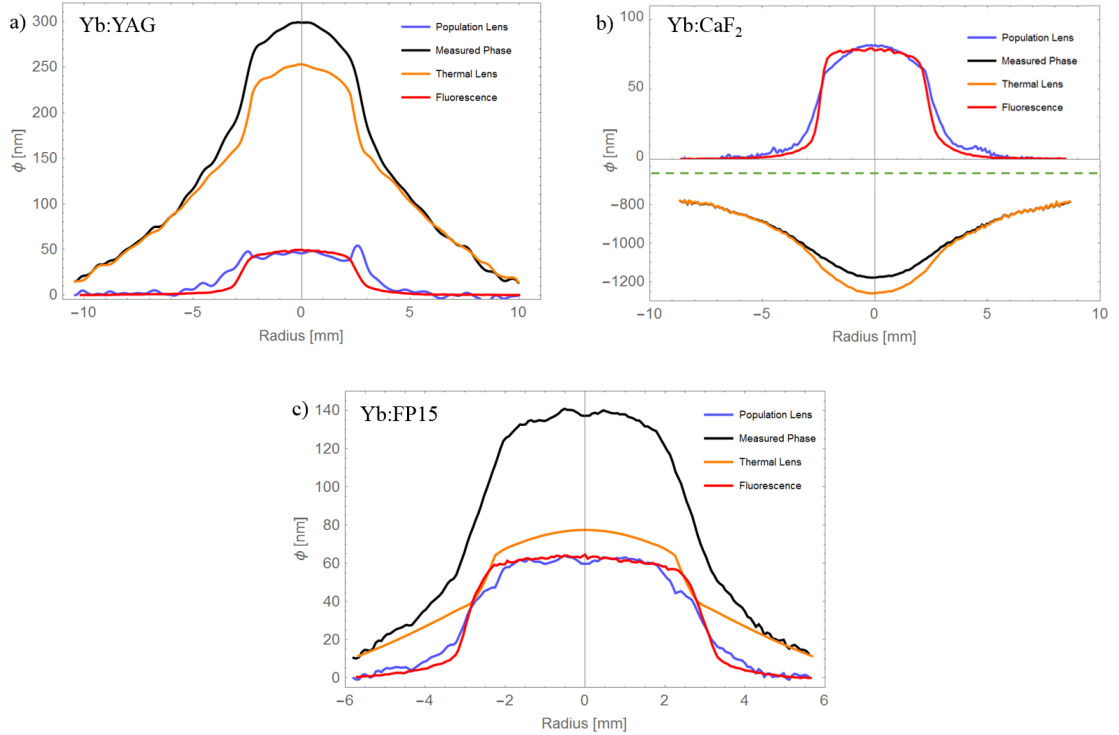

Figure 33: Spatial comparison of the measured results with the predicted superposition of the thermal and population lenses. A line-out of the fluorescence profile (red) of the active materials resembles the spatial difference ("population lens", shown in blue) of the measured phase and the simulated thermal lens.

Along with the temporal characterization of the pump-induced aberrations, the superposition of the two lens effects can also be verified spatially. Figure 33 reveals the maximum pump-induced aberrations, which occur at the end of the pump pulse for each material. Subtracting the measured (Mach-Zehnder, black) profile from the thermal lens (simulated, orange) results in the spatial profile of the population lens (calculated, blue), which matches the spatial profile of the emitted fluorescence light of the material (measured, red). The baseline of the measured phase was adjusted to match the offset of the thermal lens, since the base increase in temperature for each material produces a constant phase offset which cannot be seen through the interferometer measurements.

3.5.1   A Second-Order Phase Contribution

A discrepancy exists between the magnitudes of the thermal lens profile for the case of Yb:CaF$_2$ in figures 27b and 33b, which does not appear in the temporal plots, due to the nature of the subtracted reference (taking the thermalized reference sets the accumulated phase to zero and merely tracks the change over the pump cycle). This additional factor, extracted and displayed in figure 34, is also present in the Yb:YAG case, albeit much smaller than in Yb:CaF$_2$. The Yb:FP15 results contained no such error.
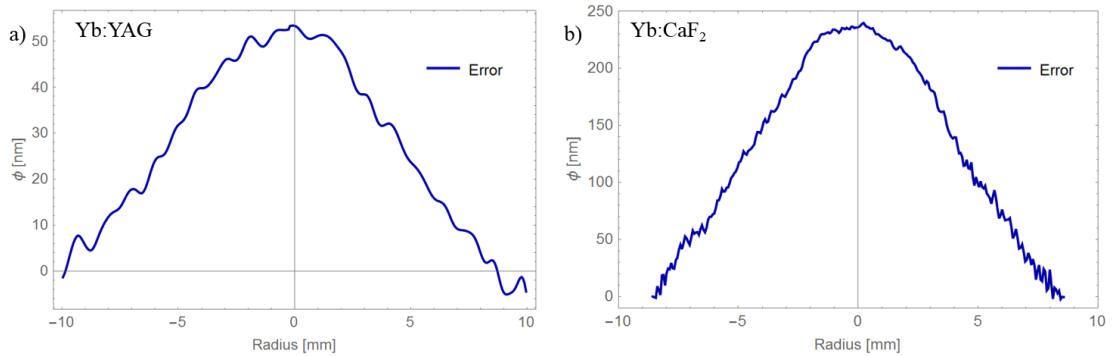

Figure 34: Second-order phase contribution for a) Yb:YAG and b) Yb:CaF$_2$.

The remaining piece of the investigation which has yet to be confirmed with measurements is the calculation of the stress and expansion. For all three active materials, a linear case was anticipated, which greatly simplifies the steps needed to model the phase-shift due to the thermal lens (a combination of the temperature-dependent refractive index, the stress-dependent refractive index, and the material expansion term). Any second-order unaccounted term has the highest chance of appearance in the Yb:CaF$_2$ results, as the magnitudes of the phase-shifts are large compared to the other two materials. It is important to note that the sign of this error is positive for both crystals, even though the thermal lenses are opposite in sign. The strongest possibility of the appearance of a positive second-order phase (which matches the parabolic shape seen above) in equation 12 is with Poisson's ratio ν, as the calculation of this parameter (which varies strongly in literature[19][28][29] for Yb:CaF$_2$) is merely a linear approximation of the ratio of material expansion along different axes ($\nu_1 \approx \frac{-\Delta d \cdot L}{\Delta L \cdot d}$, for d & Δd along the diameter, and L & ΔL along the thickness for cylindrically-shaped materials). If this second order term[33]

$$\Delta d = -d \cdot \left(1 - \left(1 + \frac{\Delta L}{L} \right)^{-\nu} \right) \Rightarrow \nu = \frac{\frac{\Delta d^2}{2d^2} - \frac{\Delta d}{d}}{\frac{\Delta L^2}{2L^2} - \frac{\Delta L}{L}} = \frac{\nu_1 \cdot (-2L + \nu_1 \Delta L)}{2L - \Delta L}, \quad (34)$$

along with the substitution of the length change due to material expansion[33]

$$\Delta L = L \cdot \alpha_T \cdot \int_0^L (T(0,z) - T(r,z))\, \mathrm{d}z = L \cdot \alpha_T \cdot \langle T(0) - T(r)\rangle, \qquad (35)$$

were to be included in equation 12, the new form for calculating the thermal lens profile becomes:

$$\phi(r) = \langle T(0) - T(r)\rangle \cdot \left[\frac{\mathrm{d}n}{\mathrm{d}T} + 2n_0^3 \alpha_T C_r' + (n_0 - 1) \cdot \right.$$

$$\left. \left(1 + \nu_1 \cdot \frac{2 - \nu_1 \cdot \alpha_T \cdot \langle T(0) - T(r)\rangle}{\alpha_T \cdot \langle T(0) - T(r)\rangle - 2} \right) \alpha_T \right]. \qquad (36)$$

This process can be modeled as well using a finite element analysis program such as COMSOL. The correction term (including the second-order expansion) is plotted below in Figure 35 against the so-called "error" term from the previous linear model. It should be noted that the discrepancy between the two terms for both Yb:YAG and Yb:CaF$_2$ is small when compared to the overall magnitudes of the phase-shift profiles.
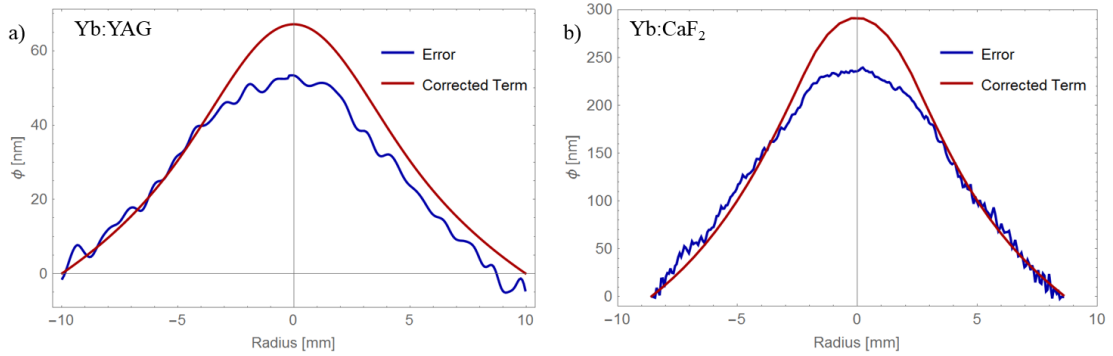

Figure 35: Correction of second-order phase contribution for a) Yb:YAG and b) Yb:CaF$_2$.

3.5.2 Dynamic Thermal Lens Competition

Another component which remains to be examined is the unexpected dip in the Yb:FP15 temporal aberration profile (figure 32c). As this behavior does not appear in the gain measurements or thermal simulation/measurements (figures 31c & 18e), a reasonable assumption is that the dip is a result of a competition between the $\mathrm{d}n/\mathrm{d}T$ and the expansion effects,[19] which share very similar magnitudes $(-8.6 \cdot 10^{-6}\,K^{-1}$ and $9.6 \cdot 10^{-6}\,K^{-1}$ respectively), yet opposite signs. The amplitude and time constant of the unknown artifact (the aforementioned "dip") can be extracted by subtracting the predicted phase-shift relaxation from the measured results to isolate the temporal profile of this effect. The sign of this additional phase-shift is both weak in magnitude and negative during the time frame from the pulse end (1.4 ms) until roughly 80 ms, where it reaches its peak value. After

this point, the effect reverts until the amplitude reaches the predicted phase-shift value at $0.5\,\mathrm{s}$. Given that the magnitude of the error is within (approximately half the value of) the difference in phase caused by the $\mathrm{d}n/\mathrm{d}T$ and expansion components of the thermal lens and changes sign, a thermal shock (rapid expansion until $1.4\,\mathrm{ms}$ and then cooling/compression thereafter) due to the large temperature spike may cause the dynamic competition between these two effects in the thermal lens. An ansatz for this additional function, which should represent the combination of the amplitudes of the $\mathrm{d}n/\mathrm{d}T$ and expansion terms ($\phi_{\mathrm{d}n/\mathrm{d}T}$ & ϕ_{α_T} respectively) along with some dynamic term as a function of the competition time τ_c, is:

$$\phi_c = \left(\chi_{\mathrm{d}n/\mathrm{d}T} + \chi_{\alpha_T}\right)\cdot\langle T(0) - T(r)\rangle\cdot t\cdot\frac{\mathrm{d}}{\mathrm{d}t}\left[e^{-t/t_c}\right] = -\left(\phi_{\mathrm{d}n/\mathrm{d}T} + \phi_{\alpha_T}\right)\cdot\frac{t}{\tau_c}e^{-t/t_c} \tag{37}$$

The competition time is assumed to be the characteristic time of this additional effect, and was determined by calculating the mean time ($50\,\mathrm{ms}$), in which the amplitude dropped to $1/e$ of its initial value. Figure 36 below displays the extracted artifact and the corrected relaxation function, which resulted in an increase in the R^2 value from 0.75 to 0.97, with an RMS error of $3\,\mathrm{nm}$. The validity of this interpretation, along with that of the second order phase contribution, remains a topic of further investigation.
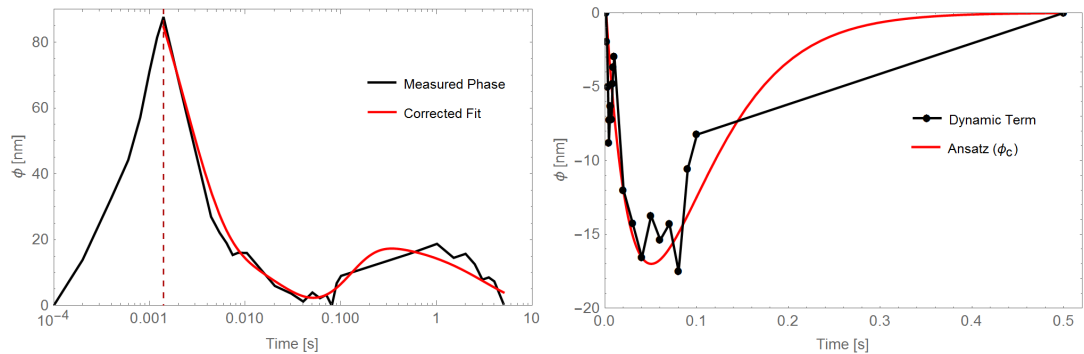

Figure 36: The corrected relaxation function (left) is produced by introducing the new phase term ϕ_c into the previous fit, which is compared to the isolated dynamic term (right).

Nevertheless, a spatiotemporal characterization has been completed in this investigation for three popular diode-pumped active materials. A convincing comparison was found between the measured phase-shift profiles and the separately determined thermal and population lens effects. The information presented in this thesis thus far is intended to contribute to a more complete picture of relevant intrinsic effects within the active material that are imbued onto the incident seed laser during the pumping process, in an effort to pave the way for improvements to state-of-the-art petawatt-class laser systems.

4   The Testbed Amplifier

A proper investigation of relevant amplification concepts benefits from the realization of a testbed amplifier. With such a system, the impact of the previously discussed pump-induced phase aberrations can be investigated within normal amplifier operation. The setup must require only a simple procedure in order to switch between different amplification schemes (free-space propagation vs. relay-imaging), active materials, various mounting types, and testing methods. There must also be a sufficient availability of space on the designated optical table for the addition of certain amplification accessories, such as spatial filters or spectral shaping mirrors. The pump source should be a high quality (high radiance and variable beam size) laser diode source, since testing diode-pumped active materials is of importance in both current and future investigations. For this reason, the pump engine, described in section 3.1, was built into the system. The construction of a folded relay-imaging amplifier allows for a variable number of passes, along with a feature in which the amplifier can bypass the curved mirrors and be "switched" into the multi-pass (free-space propagation) mode. The option of a combination of the two propagation types is available as well.

4.1   Optical Layout and Realization

The final system is described in figures 37-39. The testbed amplifier utilizes curved mirrors with focal lengths $f_1 = 1.25\,\text{m}$ and $f_2 = 0.625\,\text{m}$ respectively, leading to distances of $d_1 = 2.5\,\text{m}$ and $d_2 = 2.5\,\text{m}$, based on the folded type II relay-imaging amplifier concept detailed in section 2.1.1.1. These large distances allow for small coupling angles, while leaving enough space for the amplifier to fit within the length of the given optical table.
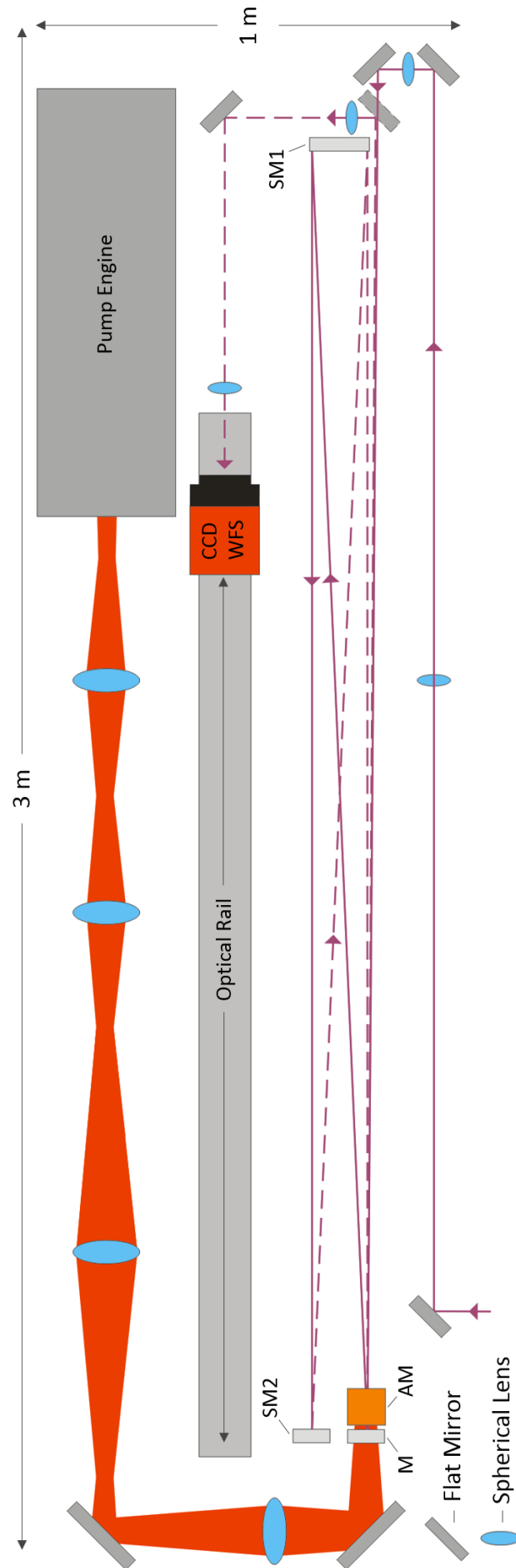
Figure 37: Schematic of the testbed amplifier setup. The path from the input beam to the first image plane (located at the dichroic mirror) is outlined in solid purple. The dashed purple lines depict the exit path. The path of the pump beam is shown in red. The dichroic mirror is denoted by "M", the mounted active material by "AM", the two spherical mirrors by "SM1" and "SM2", the camera CCD by "CCD", and the wavefront sensor by "WFS".

The setup works as follows: The seed laser is initially sent through a $400 : 750\,\mathrm{mm}$ (focal length) Keplerian telescope, one lens of which can be replaced to vary the size of the beam ($5.5\,\mathrm{mm}$ $1/e^2$ diameter), before it enters the mirror which couples the beam into the amplifier. In order to achieve the required spatial separation for in/out coupling, the input beam enters the amplifier at a height slightly higher than the center of the 3-inch mirror SM1 (seen in figure 38) and exits the amplifier at a slightly lower height.
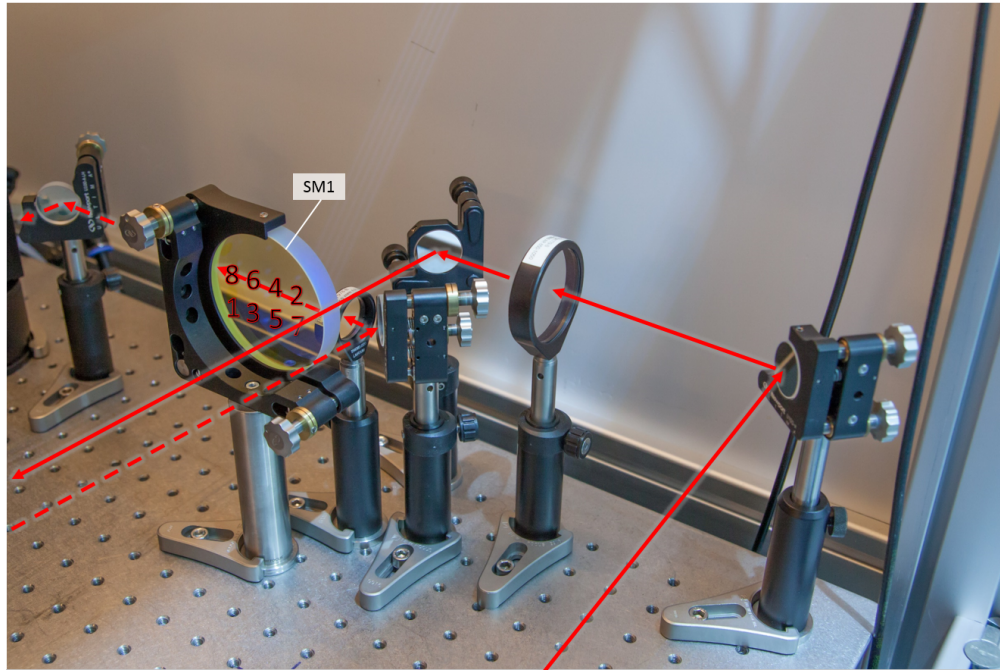

Figure 38: In/out coupling layout with input (solid red) and exit (dashed red) beam paths. "SM1" is the longer focal length ($f_1 = 1.25\,\mathrm{m}$) curved mirror. The pass orientations are numbered on the SM1 surface.

The beam then passes through the active material (figure 39), and onto the flat mirror, which acts as the first image plane of the system. The flat mirror is dichroic, which transmits the pump wavelength ($940\,\mathrm{nm}$) and reflects the seed wavelength ($1030\,\mathrm{nm}$). The pump engine (with the final $100\,\mathrm{mm}$ focal length lens replaced with a $50\,\mathrm{mm}$ focal length lens) is coupled into the amplifier using two telescopes, depicted in figure 37. One of the telescopes ($500 : 250\,\mathrm{mm}$) controls the magnification, while the other ($200 : 200\,\mathrm{mm}$) acts as a relay, to avoid physically moving the pump engine for each desired magnification. The near and far field properties of the pump engine can also be observed (for alignment purposes) within the intermediate image planes of the dual-telescope setup. The final image plane of the pump engine lies in the plane of the active material, which is placed as close as possible to the image plane of the amplifier. The material and corresponding mount can be exchanged freely (e.g., in order to test a cryogenic mount).
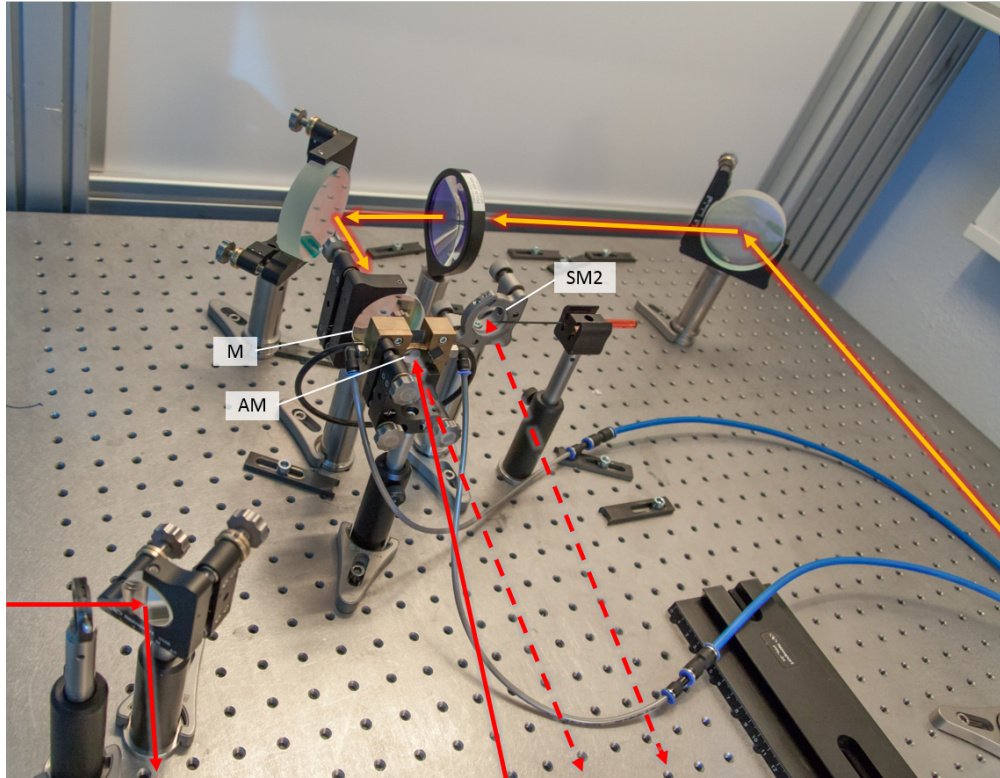
Figure 39: Imaging layout with input (solid red), exit (dashed red), and pump beam (orange) paths. "M" is the dichroic mirror which doubles as the image plane of the relay-imaging amplifier. The active material "AM" is placed directly in front of this plane. "SM2" is the shorter focal length ($f_2 = 0.625$ m) curved mirror, which can also be used to check the alignment of the amplifier.

When the seed laser reflects off of the flat dichroic mirror M, it passes through the pumped active material again and onto the 3-inch mirror SM1 (figure 38). The beam then reflects off of this mirror and forms an image onto the smaller curved mirror SM2 (figure 39), which redirects the beam onto the SM1 mirror again, finally imaging the beam onto the dichroic mirror. Through this process, the beam can be relay-imaged multiple times, with a limit dependent on the size of the beam with respect to the size of the SM1 mirror. Each round trip through the amplifier results in two passes on the SM1 mirror (numbered in figure 38), one pass on the SM2 mirror, and two passes through the active material. Through the slight rotation one of the tip-tilt knobs on the SM2 mirror, the number of passes through the relay-imaging amplifier can be varied. By rotating the flat mirror (the first image plane) towards the out-coupling mirror, the laser can bypass the relay-imaging system, and instead enter the multi-pass regime, with two passes through the active material.

A combination of relay-imaging and multi-pass (free-space propagation) can also be employed: as the laser exits through the out-coupling mirror, it passes through a telescope which images the plane of the flat mirror (the first image

plane of the relay-imaging amplifier) onto a plane located along a translation stage, which allows free-space propagation for up to roughly 1.5 m. By placing a camera on the translation stage, the change of the beam profile can be observed for a varying number of relay-imaging passes or free-space propagation distances. The camera, which grants a spatial characterization, can be easily replaced by an in-house wavefront sensor (Metrolux Shack-Hartmann WFS with corresponding Raylux software) for wavefront diagnostics. A spatial filter was installed into the system to remove high spatial frequencies from the amplified seed beam, if desired. A leakage mirror is also available, which redirects a majority of the light into a photodetector for gain measurements, while still allowing the beam profile to be observable by the camera setup.

4.2   Preliminary Characterization and Alignment Techniques

The amplifier setup was tested with an 8-pass configuration, utilizing the CW laser (enlarged to a diameter of 5.5 mm) from the gain measurements (section 3.4.2) as the seed laser. A Yb:CaF$_2$ sample was pumped by the pump engine at 6.8 kW power, 2 ms pulse duration, and 3.75 mm full beam width, which resulted in a total gain factor of 8.5 (single-pass gain of 1.3). The alignment of the pump beam in the plane of the active material was checked by imaging an Allen wrench, the shadow of which is seen in figure 40, placed very close to the surface of the material and slightly adjusting the pump engine dual-telescope system until a sharp image of both the pump beam and the Allen wrench were obtained. Testing the alignment of all passes in the amplifier was completed at both SM2 and the final exit plane.
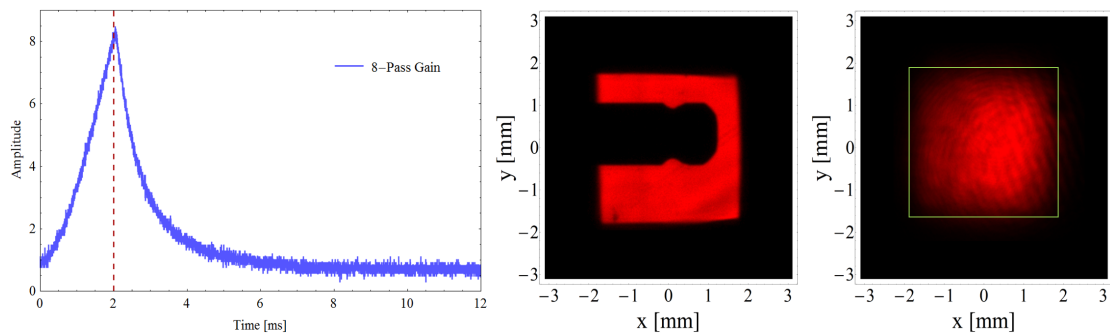

Figure 40: Initial characterization of the testbed amplifier with a 1030 nm CW TEM$_{00}$-mode laser. The 8-pass gain factor (left) was measured to be 8.5 (single-pass gain of 1.3) for a Yb:CaF$_2$ sample pumped with the 6.8 kW pump engine with a duration of 2 ms and a beam width of 3.75 mm. The center image displays the alignment of the pump engine in the plane of the active material by imaging an object (Allen wrench), which exhibits a defined shape on the same scale as the pump beam, placed very close to the material surface. The amplified (8-pass) seed laser is shown on the right.

For alignment purposes, the seed laser was made slightly larger (by 1.75 mm) than the pump beam. When the seed laser travels through the multiple passes, the portion of the seed beam which overlaps with the pump beam is amplified, while the remaining outside portion is not. This results in a "cut-out" of the pump beam onto the seed beam. When the optics within the amplifier have been aligned sufficiently, the cut-out seed beam will exhibit the same shape and size of the pump beam, except with a blurriness due to a slightly imperfect spatial overlap of the multiple passes. The low visibility fringes observed in the amplified seed laser profile are caused by the interference of the front and back reflections from the active material surface. The coherence length of the CW laser is much longer than the thickness of the active material (OPD between the front and back reflections), fulfilling the temporal coherence condition for interference. These fringes will not appear on the beam profile of the POLARIS laser pulse from the A2 setup, which can be easily coupled into the testbed amplifier through the use of a flip-mirror.

Easily variable parameters within the testbed amplifier setup include, but are not limited to: input beam size, pump fluence, pulse duration, and repetition rate, number of relay-imaging passes, length of free-space propagation, active materials and mounting conditions, additional optical components, and multiple characterization mechanisms.

5   Summary & Conclusion

Upgrades to a state-of-the-art high peak power ultrashort laser system such as POLARIS can lead to higher energies in electron or proton acceleration, or unlock new processes in laser-plasma interactions. The diode-pumped Yb^{3+}-doped active materials utilized throughout the POLARIS laser allow for high energy femtosecond pulses, but also imbue strong phase aberrations onto the seed laser, impairing the quality of the laser beam and the focal spot intensity.

The phase aberrations mainly take the form of phase-shift profiles due to pump-shaped refractive-index changes, according to the temperature distribution and level of population inversion induced through the pumping process of the materials. An investigation involving a spatiotemporal characterization of these effects was completed for three solid-state laser-active materials: Yb:YAG, Yb:CaF$_2$, and Yb:FP15. The materials were water-cooled and oriented in an end-pumping configuration. The realized pump engine is a laser diode source operating at 940 nm wavelength and 6.8 kW power at a current of 180 A. The beam profile was reshaped through the use of cylindrical dual-Keplerian telescopes and microlens arrays to produce a homogeneous square beam with a width of 1.5 cm, which was reduced to 4.5 mm using a zoom lens setup. The tested materials were pumped with pulse durations of 0.9 - 2 ms and repetition rates from 0.2 - 4 Hz.

A Mach-Zehnder interferometer captured the phase-shift profiles resulting from the thermal and population lenses with a temporal resolution of 50 μs and a spatial resolution of 65 μm/pixel. Single-pass gain measurements were used to determine the behavior of the population lens, and a COMSOL simulation was computed to estimate the thermal lens. The validity of the COMSOL simulation was confirmed by thermal measurements. Relaxation functions of the superposition of the thermal and population lenses were calculated for each material, and deviated by only ~ 5 nm (RMS) from the measured phase. The characteristic times of the population (Yb:YAG: 0.99 ms, Yb:CaF$_2$: 2.74 ms, Yb:FP15: 2.23 ms) and thermal (Yb:YAG: 0.48 s, Yb:CaF$_2$: 0.25 s, Yb:FP15: 5.02 s) lenses within the double-exponential relaxation function were matched to the fluorescence lifetime (Yb:YAG: 0.9 ms, Yb:CaF$_2$: 2 ms, Yb:FP15: 1.4 ms) and thermal diffusion time (Yb:YAG: 0.4 s, Yb:CaF$_2$: 0.35 s, Yb:FP15: 4.73 s) of the tested active materials. The polarizability difference of Yb:CaF$_2$, a parameter $(0.96 \cdot 10^{-26}$ cm$^3)$ which has yet to be published, was determined throughout the course of the investigation. The possibilities of a second order phase contribution (for Yb:YAG and Yb:CaF$_2$) and dynamic thermal lens competition (for Yb:FP15) were also investigated. The second order phase contribution was derived using a higher order expansion of

Poisson's ratio, which resulted in an updated equation for predicting the thermal lens. The dynamic thermal lens effect observed in Yb:FP15 was assumed to be a competition between the dn/dT and expansion terms in the thermo-optic coefficient, and an ansatz for the relaxation function was produced, depending on the two competing terms and the empirically determined "competition time". Including the ansatz into the previous results for Yb:FP15 increased the R^2 value of the previously calculated double-exponential fit from 0.75 to 0.97, with a reduction in the RMS error by over a factor of two ($\sim 7\,\text{nm}$ to $3\,\text{nm}$).

A testbed amplifier has been constructed in order to combine and test different amplification schemes and gain media, to determine which produce the best combination of gain, efficient energy extraction, spectral bandwidth, and resulting beam quality (wavefront aberrations), without impeding on the research endeavors of the operational POLARIS laser. With this optical system, it is also capable to observe the impact of the pump-induced phase aberrations on the profile of the seed laser beam throughout the amplification process. The amplifier design was based on the type II relay-imaging amplifier, and was characterized with a preliminary 8-pass gain measurement, using a Yb:CaF$_2$ sample pumped with the 6.8 kW pump engine with a pulse duration of 2 ms and a beam width of 3.75 mm. The seed laser was an enlarged version (5.5 mm) of the 1030 nm CW TEM$_{00}$-mode laser utilized in the gain measurements for characterizing the population lens. The resulting total gain factor was 8.5 (single-pass gain of 1.3) for the 8 passes through the material. Multiple diagnostics and accessories including a linearly-translatable (up to 1.5 m) camera/wavefront sensor (spatial/wavefront profile), photodetector (gain measurements), and spatial filter (to remove high spatial frequencies) were installed into the system.

The combination of the spatiotemporal characterization of pump-induced phase aberrations in popular Yb^{3+}-doped active materials and the completion of the testbed amplifier detailed in this thesis are intended to further advance the quality and understanding of present-day diode-pumped solid-state laser systems, and to pave the way for significant and exciting improvements on the POLARIS laser system in Jena, Germany.

Appendix: Images of Realized Measurement Configurations
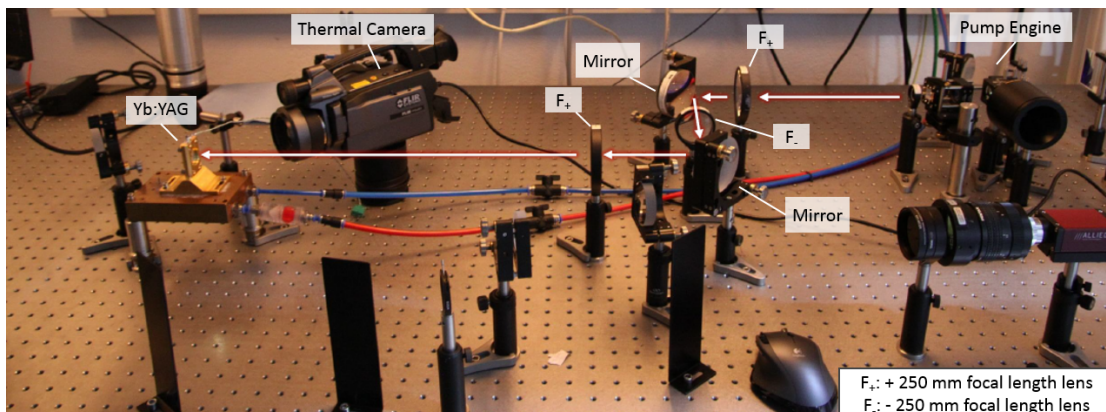

Figure 41: Illustrated photograph of the pumping configuration. The pump laser passes from the pump engine, into a zoom lens setup, and onto the active material (Yb:YAG).
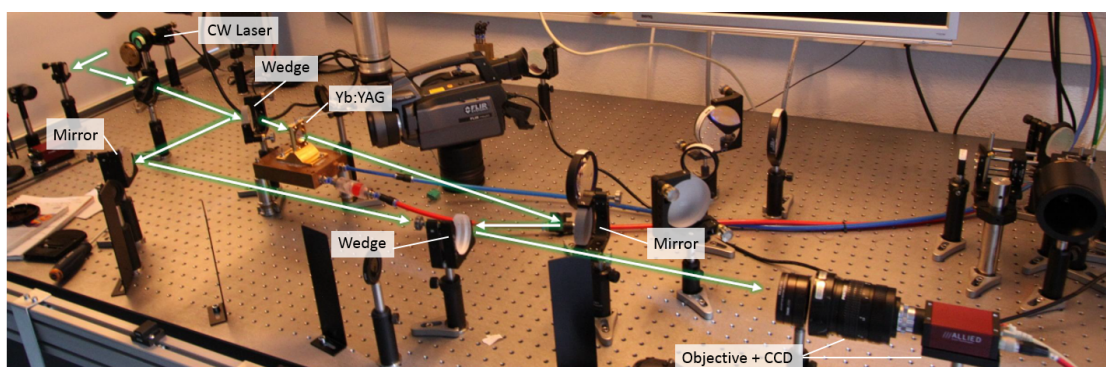

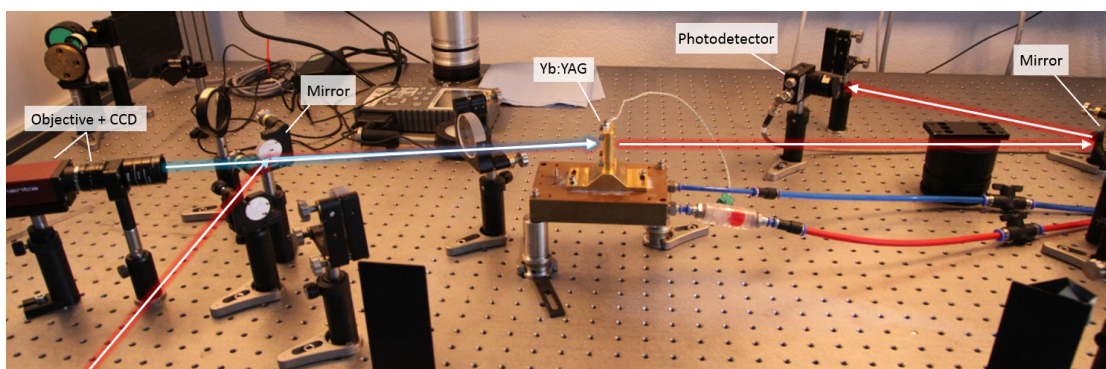Figure 42: Illustrated photograph of the Mach-Zehnder interferometer.

Figure 43: Illustrated photograph of the gain measurement setup and beam path (red). A camera was installed to view (blue) the fluorescence profile of the tested active materials.
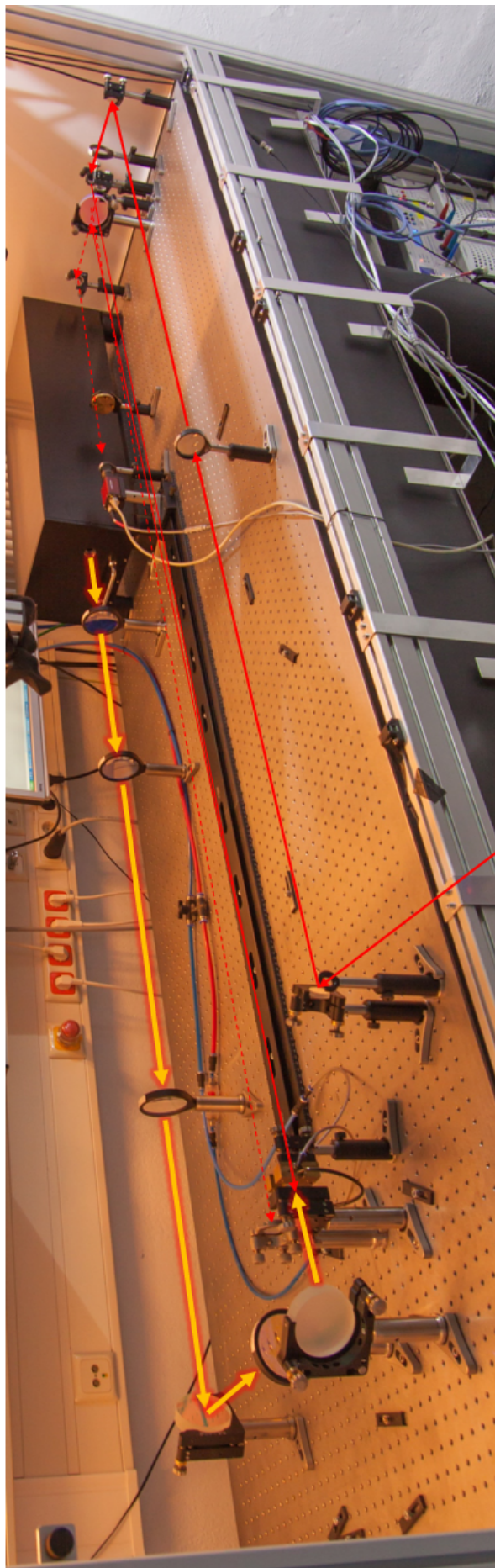
Figure 44: Full testbed amplifier setup. The path from the input beam to the first image plane (located at the dichroic mirror) is outlined in solid red. The dashed red lines depict the exit path. The path of the pump beam is shown in orange.

6   Bibliography

References

[1] C. Danson et al., High Power Laser Science and Engineering **3**, e3 (2015).

[2] A. Macchi et al., Review of Modern Physics **85**, 751 (2013).

[3] E. Esarey et al., Review of Modern Physics **81**, 1229 (2009).

[4] S. Corde et al., Review of Modern Physics **85**, 1 (2013).

[5] Y. Izawa et al., Journal of the Optical Society of Korea **12**, 178 (2008).

[6] H. Johnston, Physics World **26**, 50 (2013).

[7] M. Hornung et al., High Power Laser Science and Engineering **2**, e20 (2014).

[8] M. Hornung et al., to be published in Optics Letters, Doc. ID: 270604 (2016).

[9] O. Svelto, Principles of Lasers, 5th ed. (Springer, New York, NY, 2010).

[10] D. Strickland & G. Mourou, Optics Communications **56**, 3 (1985).

[11] C. Rulliere, Femtosecond Laser Pulses: Principles and Experiments, 2nd ed. (Springer, New York, NY, 2005).

[12] C. Wandt et al., Laser & Photonics Rev. **8**, 875 (2014).

[13] S. Nolte & M. Heinrich, Ultrafast Optics [Lecture Notes], Institute of Applied Physics, Jena, Germany.

[14] J. Körner, Effizienzsteigerung Yb^{3+}-basierter Kurzpuls-Laserverstärker, Dissertation (2014), Friedrich-Schiller-Universität Jena.

[15] M. Born & E. Wolf, Principles of Optics, 6th ed. (Pergamon Press, London, UK, 1986).

[16] B. Saleh & M. Teich, Fundamentals of Photonics, 2nd ed. (Wiley, Hoboken, NJ, 2007).

[17] M. Siebold, Hochrepetierende diodengepumpte Festkörperlaserverstärker für den Ultrakurzpulsbereich, Dissertation (2006), Friedrich-Schiller-Universität Jena.

[18] F. Dickey, Laser Beam Shaping Applications, 1st ed. (CRC Press, Boca Raton, FL, 2005).

[19] Chénais et al., Progress in Quantum Electronics **30**, 4 (2006).

[20] Frank Traeger, Springer Handbook of Lasers and Optics, 1st ed. (Springer, New York, NY, 2007).

[21] A. Cousins, IEEE Journal of Quantum Electronics **28**, 4 (1992).

[22] O. L. Antipov et al., Optics Letters **31**, 6 (2006).

[23] M. V. R. K. Murty, Applied Optics **3**, 4 (1964).

[24] G.S. Sarkisov, Instruments and Experimental Techniques 39, 5 (1996).

[25] M. Takeda et al., Journal of the Optical Society of America **72**, 1 (1982).

[26] FLIR Systems, High speed thermal cameras, (2016).

[27] Hellma Materials, CaF2 data sheet, (2012).

[28] F. Druon et al., Optical Materials Express **1**, 3 (2011).

[29] J. Boudeile et al., Optics Express **16**, 14 (2008).

[30] C. Jacinto et al., Journal of Non-Crystalline Solids **352**, 32-35 (2006).

[31] T. Töpfer, Diodengepumpte Hochleistungsglaslaser - Lasermaterialien, Pumplaserdioden und Verstärker für den POLARIS-Laser, Dissertation (2001), Friedrich-Schiller-Universität Jena.

[32] J. Körner et al., Journal of the Optical Society of America B **29**, 9 (2012).

[33] R. Budynas & J. Nisbett, Shigley's Mechanical Engineering Design, 8th ed. (McGraw-Hill, New York, NY, 2006).

Danksagung

An dieser Stelle möchte ich mich bei allen bedanken, die zum Gelingen dieser Masterarbeit beigetragen haben. Mein besonderer Dank gilt

- **Prof. Malte C. Kaluza** für die Vergabe des interessanten Themas sowie für seine Zeit, die er schon während dieser zwei Jahren verbraucht hat, um meine Fragen zu beantworten und über viele wichtige Sache zu diskutieren. Bevor ich nach Jena angekommen bin, konnte ich mich nicht vorstellen, dass ich mit solchen interessanten Projekten mich beschäftigen könnte, als was die relativistische Laserphysik Forschungsgruppe anbietet.

- **Dr. Marco Hornung** für seine Betreuung und fantastische Arbeitseinstellung. Man findet kaum einen Menschen, der sich darum kümmert, einen Student zu fragen, ob er völlig zufrieden mit seinem Projekt ist.

- **Sebastian Keppler** für die kontinuierliche Unterstützung und viele Erklärungen, wann es insbesondere mal wieder länger gedauert hat. Dank ihm habe ich wirklich sehr viel gelernt.

- **Dr. Jörg Körner** für seine umfassende Expertise, die er mit mir geteilt hat.

- **Matthew Schwab** für seine sehr hilfreiche Anwesenheit während meines gesamten Masterstudiums. Wenn wir uns vor zwei Jahren nicht über Skype unterhalten hätten, hätte ich mich nicht dazu entschlossen, aus Tucson nach Jena zu ziehen.

- **Georg Becker** für die vielen tollen Empfehlungen und lustigen Gesprächen.

- **Szilvia Mammel** für ihr stets offenes Ohr für alle Fragen und Sorgen, die ich hatte.

- **Den gesamten POLARIS- und RLP-Arbeitsgruppen** für das angenehme Betriebsklima.

- **alla mia ragazza Letizia D'Amico** per l'insostituibile compagnia (e letizia) che mi ha regalato negli ultimi due anni e in anticipo per gli anni a venire.

Most of all, I would like to thank my mother Marlene Hanna and brother Issam Tamer, who have 100% supported me throughout all of my endeavors, regardless of how crazy or difficult they were (even if it meant traveling over 5000 miles, across an ocean, to a country where I had no prior knowledge of the native language, just to be a part of the field I'm passionate about). I'm greatly indebted to you both.

Declaration of Authorship

I hereby certify that this thesis has been composed by me and is based on my own work. Any other aids and sources have been treated with due acknowledgement. I further declare that I have not submitted this thesis at any other institution in order to obtain a degree.

_____   Jena, November 11, 2016